











Revealing the Transition Region of QCD with the Proton's g_2 Structure Function (PAC53)

Anchit Arora, Hector Chinchay, Muhammad Farooq, Chhetra Lama, Elena Long ,
Michael McClellan, Olaiya Olokunboyo, David Ruth[†] , Nathaly Santiesteban* ,
Karl Slifer* , Zoe Wolters, and Allison Zec 

University of New Hampshire, Durham, NH 03861

James Brock, Alexandre Camsonne , Jian-Ping Chen* , Silviu Covrig Dusa,
Alexandre Deur , Dave Gaskell , Mark Jones, Chris Keith, Dave Mack,
James Maxwell , Dave Meekins, and Arun Tadepalli

Thomas Jefferson National Accelerator Facility, Newport News, VA 23606, USA

Ishara Fernando, Dustin Keller, Michael Nycz, Oscar Rondon-Aramayo, and
Jixie Zhang

University of Virginia, Charlottesville, VA 22904

Whitney Armstrong, Sylvester Joosten, Zein-Eddine Meziani, and Chao Peng

Argonne National Laboratory, Lemont, IL 60439

Hamza Ataç, Nazmus Ifat, Suman Shrestha, and Nikos Sparveris

Temple University, Philadelphia, PA 19122

Sebastian Kuhn and Pushpa Pandey

Old Dominion University, Norfolk, VA 23529

Garth Huber

University of Regina, Regina, SK S4S0A2, Canada

Pete Markowitz

Florida International University, Miami, FL 33199

Darko Androic

University of Zagreb, Faculty of Science, Croatia

Axel Schmidt

George Washington University, Washington, DC 20052

Simon Širca

Faculty of Mathematics and Physics, University of Ljubljana, Slovenia

*: Co-spokesperson, †: Contact-spokesperson (david.ruth@unh.edu)

Executive Summary

In this experiment, we propose to measure the g_2 spin structure function of the proton in the transition region of QCD, and extract its moments, with a focus on the \bar{d}_2 polarizability and the hyperfine structure contribution Δ_2 , as well as quantify the twist-3 effects described by \bar{g}_2 . This measurement provides the unique chance to benchmark Lattice QCD in the regime where both perturbative QCD and effective theories break down, study difficult-to-access higher twist effects, and reduce the leading uncertainty in calculations of the hydrogen hyperfine splitting. We will collect a high-precision result for g_2 and its moments over a full order of magnitude in Q^2 from 0.22 - 2.2 GeV². g_2 has never before been directly measured for either nucleon in this regime, so this experiment presents the best and currently only chance to quantify this fundamental nucleon observable in the transition region.

This experiment will be conducted in Jefferson Lab's Hall C using the SHMS spectrometer and a transversely polarized proton target. We require the standard Hall C equipment package, with the addition of the aforementioned polarized target and a set of chicane magnets designed by Dr. Jay Benesch to compensate for the bending of the beam in the transverse target field. The chicane which will be needed for the current beamline geometry is nearly identical to those used many times in previous transverse polarized target experiments in both Hall A and Hall C. Our collaboration includes members from many of these experiments and we intend to use this legacy expertise to repeat our past successes with this experimental setup.

The experiment requires beam energies of 4.4 and 8.8 GeV, with 80 nA current. This current level is required to maintain stable target polarization. We require 13 PAC days to perform a high precision measurement of g_2 , and an additional 13 days of overhead primarily needed to successfully operate the polarized target. **Therefore, we request a total of 26 days to perform the full experiment.**

New Changes from PAC Comments

PAC-52 previously recognized the strong physics motivation of this proposal and conditionally (C2) approved it in 2024, with the requirement that we perform a simulation evaluating the impact of the chicane and target field on the detector resolution and experimental observables to obtain full approval.

This document details the results of the simulation, which is based on previous analyses of the small acceptance spectrometers in Hall A & C, and which provides a full understanding of effects from the target field and chicane, significantly strengthening the proposal. The impact of the target and chicane on the resolution and experimental observables is now thoroughly quantified. As will be shown below, the effect of the target field and chicane is now very well understood, at a level that no other polarized target experiment at Jefferson Lab has developed prior to the start of the experiment. The proposal is significantly strengthened by this new simulations work, and the impact of the equipment on the resolution and physics of the experiment is now thoroughly quantified.

We summarize here the major changes between this proposal and the previous version:

- **Section 5 has been added detailing the new work on the simulation procedure, and the results on the kinematic coverage and resolution. We find that the impact on the resolution is small compared to the experimental bin size, the kinematic coverage is not effected significantly, and the effects of the target field and chicane, which are small in comparison to our dominating systematics, are now thoroughly quantified in the error analysis and rates calculation of the experiment.**
- Based on verbal discussions at PAC-52, we have clarified our goal for g_2 's first moment Γ_2 by moving discussion of this moment out of the primary physics motivation and into Section 3.7 as a tool to constrain the low- x part of the other moments.
- A calculation on multiple scattering effects previously requested by the TAC has been added in Section 3.6.
- More information on the target mass corrections procedure, including the approximate magnitude has been included in Section 4.
- We have added clearer plots and more explicit descriptions of the low- x analysis in Section 3.7, demonstrating explicitly that the measured region should cover nearly the entire expected value for desired moments at the kinematic settings of this proposal.
- PAC52 had a concern that the chicane was a 'proof of principle' design. We have added information on new Chicane optimizations and simulations performed by Dr. Ryan Bodenstein and Dr. Jay Benesch. The relevant tech notes are attached at the end of the proposal, which demonstrate that the necessary chicane configuration is very similar to the designs used for the SANE, g2p, GeP and RSS experiments, and should be completely feasible given an appropriate time investment to set it up.
- We have attempted to clarify and improve descriptions of the experiment and its goals throughout the proposal.

This simulations work fulfills the condition provided by PAC-52, and we believe that this iteration of the proposal presents the strongest possible case that it is time for the experiment to be fully approved. We are ready and eager to move forward with preparing to run this exciting and necessary experiment, and we hope you find this opportunity as exciting as we do.

Contents

1	Introduction	4
2	Physics Motivation	5
2.1	Higher Twist Probes	6
2.2	Transverse Spin Structure PDF g_T	6
2.3	\bar{d}_2 Polarizability	6
2.4	Hydrogen Hyperfine Structure Contribution	8
3	Experimental Details	9
3.1	Required Equipment	11
3.1.1	Polarized Target	11
3.1.2	Chicane	11
3.1.3	Raster	12
3.1.4	Exit beam pipe and beam dump	12
3.2	Beamline Instrumentation	12
3.2.1	Beam Current and Beam Charge Monitor	12
3.2.2	Beam Polarimetry	13
3.2.3	The Spectrometers	13
3.2.4	Detector Stack	13
3.3	Synchrotron Radiation	13
3.4	Optics	13
3.5	Data Acquisition	14
3.6	Multiple Scattering	14
3.7	Low-x Contributions	14
3.8	Statistics and Systematics	16
3.9	Kinematics	17
4	Analysis Method	24
4.1	Extraction of the g_2 Structure Function	24
4.2	Interpolation to Constant Q^2	26
5	Simulation Results	27
5.1	Hall A/C Simulation Procedures & Simulation Details	27
5.2	Simulation Output	28
6	Beamtime Request	32
6.1	Overhead	33
7	Summary	35
	Supplemental Materials	39
	Dr. Ryan Bodenstein - Bmad Chicane Simulation Technote	39
	Dr. Jay Benesch - Preliminary Chicane Technote	39

1 Introduction

The g_2 spin structure function is a quantity which can be derived in spin- $\frac{1}{2}$ systems which, along with its twin g_1 , provides information on how the nucleon's spin structure varies from point-like behavior at constant Q^2 . Further, these quantities are extremely important because they can be integrated to construct moments which can be derived directly from theoretical predictions. Consequently, measurements of the spin structure functions enable direct comparison between experimental measurements and their matching theoretical frameworks. At low Q^2 , this provides a means to test effective theories of Quantum Chromodynamics (QCD) such as Chiral Perturbation Theory (χ PT). And specifically, in the transition region targeted by this proposal, they can be used to benchmark upcoming predictions of Lattice QCD [1] which will help to bridge the gap between perturbative QCD and the realm of effective theories.

If we define $q_f(x)dx$ { and $\bar{q}_f(x)dx$ } as the expectation value for the number of quarks { and anti-quarks } of flavor f in the hadron whose momentum fraction lies in the interval $[x, x + dx]$, then in the parton model we can define the unpolarized structure function F_1 as:

$$F_1(x) = \frac{1}{2} \sum_f z_f^2 (q_f(x) + \bar{q}_f(x)) \quad (1)$$

We can also write a spin-dependent structure function, wherein $\Delta q_f(x) = q \uparrow(x) - q \downarrow(x)$ represents the difference between helicity aligned and antialigned quarks with respect to the overall longitudinal nucleon spin, and $\Delta \bar{q}_f(x)$ represents the antiquark equivalent:

$$g_1(x) = \frac{1}{2} \sum_f z_f^2 (\Delta q_f(x) + \Delta \bar{q}_f(x)) \quad (2)$$

Here, the quark charge z_f enters due to the fact that the cross section is proportional to the squared charge of the target. The Callan-Gross [2] relation shows that unpolarized structure function F_2 can be defined entirely in terms of F_1 , but there is no such simple partonic interpretation of g_2 . Instead, this spin-dependent structure function is determined by the x -dependence of the quarks' transverse momenta and the off-shellness, both of which are unknown in the parton model [3].

Ignoring quark mass effect of order $\mathcal{O}(m_q/\Lambda_{QCD})$, g_2 can be separated into leading and higher-twist components as:

$$g_2(x, Q^2) = g_2^{\text{WW}}(x, Q^2) + \bar{g}_2(x, Q^2) \quad (3)$$

where

$$\bar{g}_2(x, Q^2) = - \int_x^1 \frac{\partial}{\partial y} \left[\frac{m_q}{M} h_T(y, Q^2) + \zeta(y, Q^2) \right] \frac{dy}{y} \quad (4)$$

To twist-3, there are three contributions to g_2 :

1. g_2^{WW} : The leading twist-2 term, which depends only on g_1 .
2. h_T : Arises from the quark transverse polarization distribution. Also twist-2, this term was long expected to be suppressed by the smallness of the quark mass.
3. ζ : The twist-3 part which arises from quark-gluon interactions.

There has been a significant amount of in-depth analysis of the latter two terms in recent years [4, 5].

The Wandzura–Wilczek [6] relation:

$$g_2^{\text{WW}}(x, Q^2) = -g_1(x, Q^2) + \int_x^1 \frac{dy}{y} g_1(y, Q^2) \quad (5)$$

describes the leading twist part of the g_2 completely in terms of g_1 . In reality, Eq. 5 is a good approximation of g_2 only at large Q^2 . At low Q^2 kinematics, g_2 exhibits strong deviations from leading twist behaviour. This gives g_2 a unique sensitivity to higher twist, *i.e.* interaction-dependent effects in QCD [3]. This sensitivity makes it an ideal quantity for studying the transition region, where quark-gluon correlations dominate and higher twists begin to contribute.

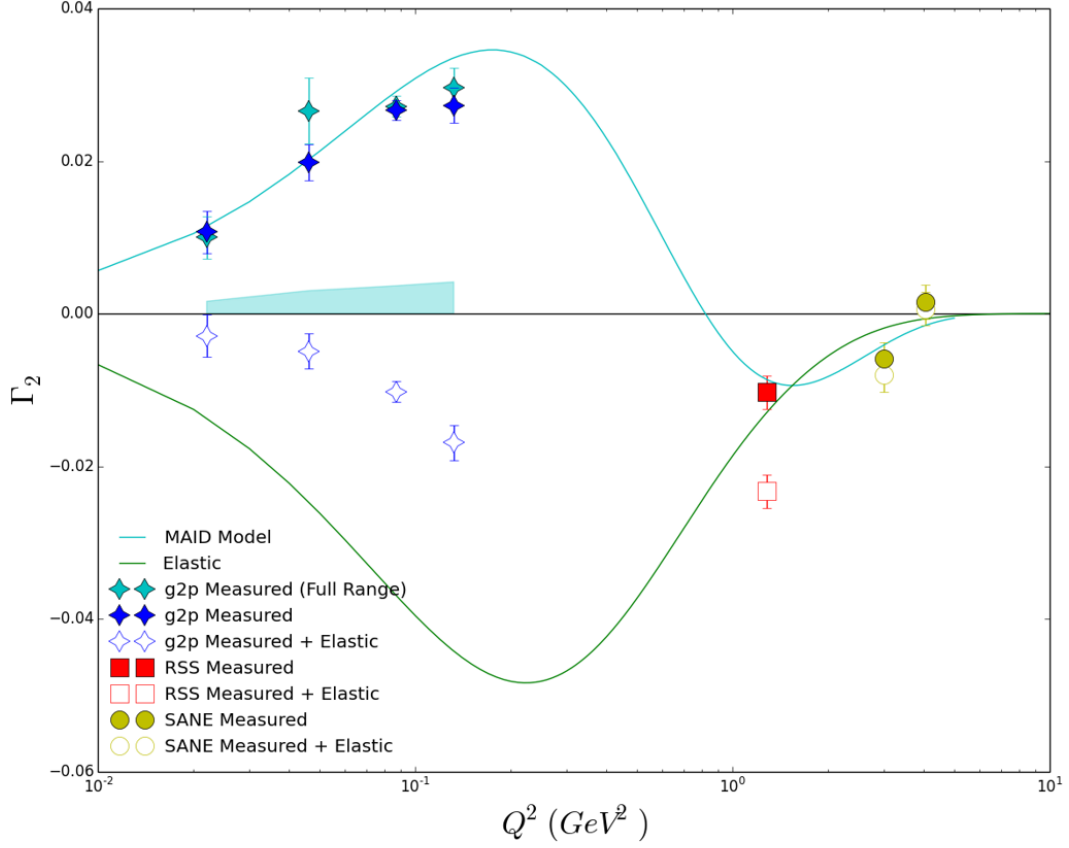


Figure 1: The Γ_2 moment. Light blue points represent an integral of the full measured region of E08-027, while dark blue points are limited to a maximum W of 1725. The MAID phenomenological model [7] is also run over this limited W range, as are the other experiments' results, to provide an even comparison. Results of RSS [8] are shown in red, and results of SANE [9] are shown in yellow. The open symbols represent the sum of the measured and elastic parts of the integral, excluding only the unmeasured high- W part.

2 Physics Motivation

As is clear from the above, g_2 is an ideal quantity for probing the transition region, which is arguably the least well understood regime in QCD due to the relative breakdown of both chiral effective theory and perturbative QCD. This fundamental observable can be used as a tool to study quark-gluon correlations and higher twist, but also has even more power when combined with its twin g_1 : together, the spin structure functions can be integrated to form polarizabilities which are directly calculable by theories of QCD. In the transition region, especially relevant is the chance to directly benchmark Lattice QCD, currently one of the best prospects for bridging the perturbative QCD and effective theory worlds.

g_2 of the proton has previously been measured several times at Jefferson Lab, primarily in Hall C and Hall A through the use of a transversely polarized target and chicane magnets. These experiments, E08-027, SANE, and RSS, obtained high precision results in the high and low Q^2 regimes but have left an order-of-magnitude-wide hole in world coverage of this quantity in the intermediate Q^2 transition regime. The Q^2 coverage can be most easily seen by inspecting g_2 's first moment, $\Gamma_2 = \int_0^1 g_2(x, Q^2) dx$, shown in Figure 1.

Though this quantity has never before been measured in the transition region, this regime hosts a wealth of possibilities for understanding QCD and nucleon structure. Below, we discuss the important quantities which can be extracted from g_2 , which together make a transition region measurement of this quantity a necessity to complete our understanding of the nucleon and the strong force.

2.1 Higher Twist Probes

Before discussing the value of moment integrals derived from this structure function, it is worthwhile to consider g_2 's power as a fundametable nucleon observable. At this point, a significant amount of g_1 data exists for the proton over a broad kinematic spectrum [10, 11], meaning that the g_2^{WW} term of g_2 is well understood and can be estimated with a model or with world data. A precision measurement of $g_2(x, Q^2)$ can then subtract this term to obtain a measurement of the \bar{g}_2 term above. Bag model calculations [12, 13] indicate a significant twist-3 component of g_2 , making this observable's study in the transition regime extremely interesting: twist-3 effects are poorly understood in general, and a continuous \bar{g}_2 spectrum can allow us to better quantify their magnitude as we move from leading twist at high Q^2 to higher twist and the eventual breakdown of the twist approximation at intermediate and low Q^2 , which would provide us with new information on quark-gluon interactions [4].

2.2 Transverse Spin Structure PDF g_T

We can also use both polarized spin structure functions to define a combined transverse spin structure function:

$$g_T = g_1 + g_2 \quad (6)$$

This structure function can be useful in several important ways. Firstly, direct measurements of the structure functions are inherently limited by the experimental inability to obtain total x -coverage, as doing so would require an infinitely high invariant mass W to completely quantify the low- x behaviour of the structure functions. But for g_1 , interesting progress has been made on quark helicity evolutions to low- x [14]. For the flavor-singlet helicity part of g_1 , the 2017 result of Kovchegov, Pitonyak, and Sievert reads:

$$g_1^S(x, Q^2) \approx \left(\frac{1}{x}\right)^{2.31\sqrt{\frac{\alpha_s N_c}{2\pi}}} \quad (7)$$

wherein α_s is the QCD strong coupling constant and N_c is the number of colors. There is notable interest in extending the techniques used to obtain this result to g_T , a prospect which requires a complete spectrum of g_2 results to match the impressive completeness of available g_1 data [4]. Employing these evolutions on a completed data-set of g_T may allow us to better understand the difficult to access small- x regime of nucleon structure for all Q^2 .

The combination function g_T is also notable because it can be connected to the Transverse Momentum Dependent (TMD) distribution function g_T^\perp [15]:

$$g_T = \int d^2 k_T [g_T' - \frac{k_T^2}{2M^2} g_T^\perp] \quad (8)$$

This provides a promising opportunity to link inclusive spin structure function measurements with semi-inclusive deep-inelastic extractions of the TMDs, which describe the nucleon's structure as a function of the transverse parton momentum k_T and longitudinal momentum fraction x .

2.3 \bar{d}_2 Polarizability

Sum rules involving the spin structure of the nucleon offer an important opportunity to study QCD. In recent years the Bjorken sum rule at large Q^2 , and the Gerasimov-Drell-Hearn (GDH) sum rule [16] at $Q^2 = 0$, have attracted a concerted experimental and theoretical effort (see for example [17]). Another class of sum rules address the generalized GDH sum [18] and the spin polarizabilities [19]. These sum rules which are based on unsubtracted dispersion relations and the optical theorem relate the moments of the spin structure functions to real or virtual Compton amplitudes, which can be calculated theoretically.

At large Q^2 , it is possible to apply the Operator Product Expansion (OPE) to the forward virtual Compton scattering amplitude, yielding the d_2 matrix element: a spin structure function moment related to the color polarizabilities, which describe how the color electric and magnetic fields respond to the nucleon spin (see for example [20]). At lower momentum transfer, a moment identified with this matrix element, $\bar{d}_2(Q^2)$, provides a means to study the transition from perturbative to non-perturbative

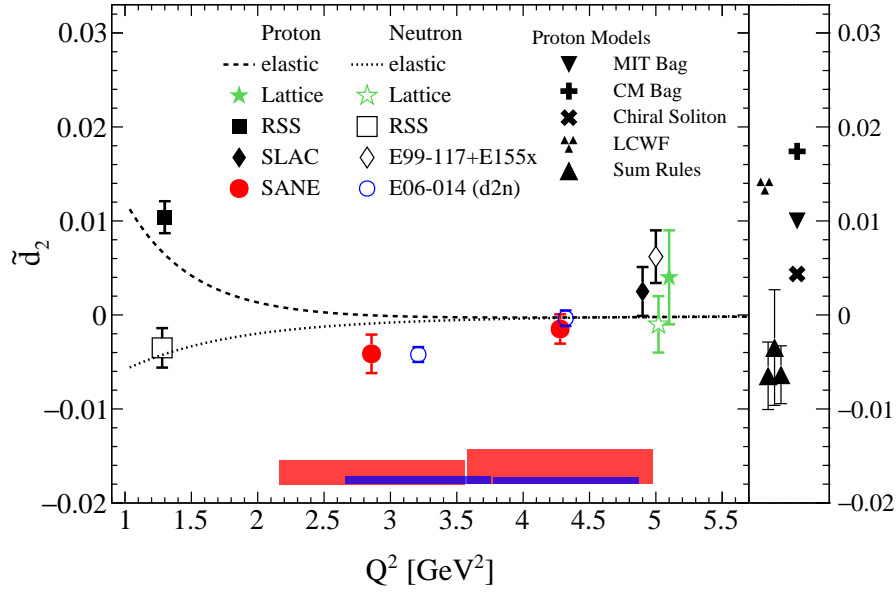


Figure 2: \bar{d}_2 of the proton from SANE and recent neutron results [22]. Also shown are the lattice QCD results [23], previous proton (neutron) measurements with filled (open) symbols from SLAC [24], E99-117 and E155x [25], and *RSS* [26, 27] experiments. The dashed (dotted) lines show the elastic contribution for the proton (neutron). The panel on the right shows proton model calculations from QCD sum rules [28], the bag model [29], the Center-of-Mass (CM) bag model [30], the chiral soliton model [31], and light-cone wave functions (LCWF) [13].

behaviour and to quantify higher twist effects via:

$$\bar{d}_2(Q^2) = 3 \int_0^1 x^2 [g_2(x, Q^2) - g_2^{WW}(x, Q^2)] dx \quad (9)$$

The lowest twist component in d_2 is twist-3, and higher twists can contribute at low Q^2 . And although d_2 is a higher-twist OPE object, the definition of \bar{d}_2 holds for all Q^2 . Then d_2 is just the x^2 moment of the difference between g_2 and g_2^{WW} even at low momentum transfer, such that it may be referred to as the twist-3 operator. It must vanish for $Q^2 \rightarrow 0$, and $Q^2 \rightarrow \infty$ but peaks around 1 GeV^2 . In this sense, it represents a measure of QCD complexity and is of significant interest to map out d_2 over the transition region where this complexity is maximized.

Previous measurements of \bar{d}_2 are shown in figure 2. The Spin Asymmetries of the Nucleon Experiment (SANE) [9] measured g_2^p and the d_2^p matrix element for $0.3 < x < 0.8$. The twist-3 matrix element, d_2^p , is proportional to an average color Lorentz force, and was extracted from the measured asymmetries at Q^2 values ranging from 2.0 to 6.0 GeV^2 . The data surprisingly display the opposite sign compared to most quark models, including the lattice QCD result. The SANE data also has the opposite sign to the RSS and E08-027 measurements. Ref. [9] notes that when compared to the neutron data in the same Q^2 range their results suggest a flavor independent average color Lorentz force. The RSS and SANE points for this moment are calculated as a Nachtmann moment [8, 21], incorporating potentially large target mass corrections that are ignored in the Cornwall-Norton moment of 9.

Fig. 3 shows the Q^2 evolution of the proton d_2 to lower Q^2 . E155x [24] provides one point at an average Q^2 of 5.0 GeV^2 and RSS [8] measured d_2^p at $Q^2 \approx 1.3 \text{ GeV}^2$. The large shaded area represents the global analysis of Osipenko et al. [32] using the existing g_1^p data [34] and the MAID [7] model. However, the MAID model disagrees strongly with the existing data, and the authors of [32] note that ‘new experimental data on g_2 in the resonance region at different Q^2 values are clearly needed’.

The transition region is the only QCD regime still essentially devoid of data on \bar{d}_2 , and it is imperative to understand its behavior. In particular, as shown in figures 2 and 3, this is an ideal

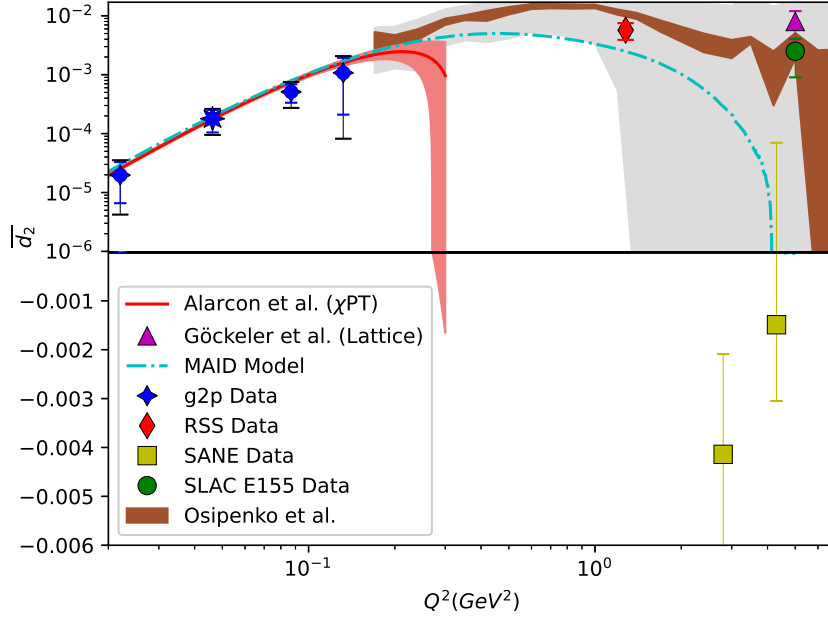


Figure 3: $\overline{d_2}$ for the proton as a function of Q^2 , compared to existing data [8, 24, 9], the phenomenological models [7, 32], χ PT calculations [33] and a Lattice QCD calculation [23]. The region above zero is shown on a log scale on the y axis to clearly show the comparison with the model, while the negative half of the plot is shown on a linear scale to allow the proper inclusion of the SANE [9] data.

quantity for testing Lattice QCD, which is currently one of the best hopes of understanding the transition regime. New Lattice calculations of $\overline{d_2}$ are expected in the next few years, which will require a benchmark from the experimental data collected by this experiment.

2.4 Hydrogen Hyperfine Structure Contribution

The hyperfine structure of the hydrogen atom has been experimentally measured with extreme precision in atomic physics, but there are large uncertainties remaining in the theoretical approach. These are driven by a lack of understanding of the proton's internal structure, which contributes to the two-photon contribution to hyperfine splitting [35]:

$$E_{nS-hfs}^{2\gamma} = \frac{E_F}{n^3} \left(\Delta_Z + \Delta_{recoil} + \Delta_{pol} \right) \quad (10)$$

Here the Δ_Z and Δ_{recoil} terms represent the Zemach radius and recoil contributions, and E_F is the Fermi energy. Relevant to the discussion of this proposal, the Δ_{pol} term represents contributions from the proton's internal structure, split into two other contributions, Δ_1 and Δ_2 :

$$\Delta_{pol} = \frac{\alpha m_e}{\pi g_p M_p} \left(\Delta_1 + \Delta_2 \right) \quad (11)$$

This term accounts for nearly 70% of the uncertainty in the calculations of hyperfine splitting [36]. The second of its two terms can be written in terms of the g_2 structure function which this experiment aims to measure:

$$\Delta_2 = -24 M_p^2 \int_0^\infty \frac{dQ^2}{Q^4} \int_0^{x_{th}} \tilde{\beta}_2(\tau) g_2(x, Q^2) dx \quad (12)$$

Where $\tilde{\beta}_2$ is a kinematic factor which depends on x and varies between electronic and muonic hydrogen with the mass of the lepton. Though much of the strength of this contribution is at lower Q^2

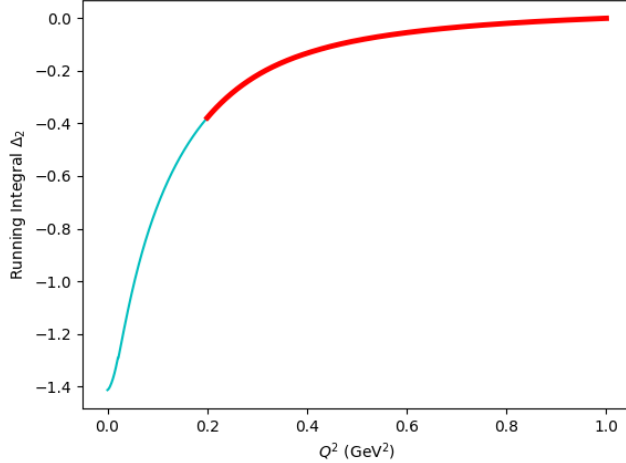


Figure 4: Running integral of the Δ_2 contribution to hyperfine splitting in muonic hydrogen, from high to low Q^2 . The red line represents the region covered by this proposal, while the cyan region represents the rest of the integral.

due to the strong $\frac{1}{Q^4}$ weighting of the integral, existing data and models expect a significant amount of strength remains in the region $0.22 < Q^2 < 1.0 \text{ GeV}^2$, necessitating further measurement in this region for a complete understanding of atomic hyperfine structure. As can be seen in Figure 4, the transition region which this proposal aims to measure accounts for around 30% of the total value of Δ_2 , based on a running integral from high to low Q^2 of the MAID phenomenological model prediction for this quantity [7]. Δ_2 accounts for around 28% of Δ_{pol} , and Δ_{pol} remains the dominating theoretical uncertainty in the overall hyperfine splitting calculation, accounting for nearly 70% of the current uncertainty [36, 35]. Therefore, although there is a six-order-of-magnitude gap between experimental and theoretical precision for the hyperfine splitting, the theoretical precision cannot improve by more than one order of magnitude without a precision g_2 measurement in the transition region.

Perhaps the strongest motivation to study this region comes from the results of Jefferson Lab E08-027, which discovered a more significant Δ_2 contribution at low Q^2 than was previously expected. The result of this experiment reduced a large and long-standing tension between theory and experiment for the value of Δ_{pol} [35, 37]. If Δ_2 proves to also be larger than phenomenological models predict in the transition region, as was found to be true at low Q^2 , it could further reduce or eliminate this tension. Consequently, obtaining a precise measurement of Δ_2 over the transition region is crucial for the study of nuclear and atomic physics, and will further shrink the uncertainty on calculations of hyperfine splitting in electronic and muonic hydrogen.

3 Experimental Details

We plan to perform an inclusive measurement at forward angle of the proton spin-dependent cross sections in order to determine the proton's g_2 structure function in the resonance region for $0.22 < Q^2 < 2.2 \text{ GeV}^2$. The kinematic coverage, shown in Fig. 5, complements recently published experiment EG4 [38] and will fill in a significant hole in world data for transversely polarized protons. The data is focused in the unmeasured region between the RSS [8] and g2p [39] experiments, but also includes two kinematic settings with higher beam energies aimed to fill in the unmeasured region between RSS and SANE [21]. This higher Q^2 data will help to further investigate the interesting result of the SANE experiment [21] discussed in the previous section, and along with the lower Q^2 data, fill the last gaps in a continuous Q^2 spectrum of g_2 data from 0.01 to 20 GeV^2 . All settings will measure data with a transversely polarized target following the procedures that proved successful during the E08-027 (g2p) [39] experiment. Due to the need for very small scattering angles at a beam energy of 4.4 GeV, and a larger central momentum at a beam energy of 8.8 GeV, data will be taken only with the SHMS.

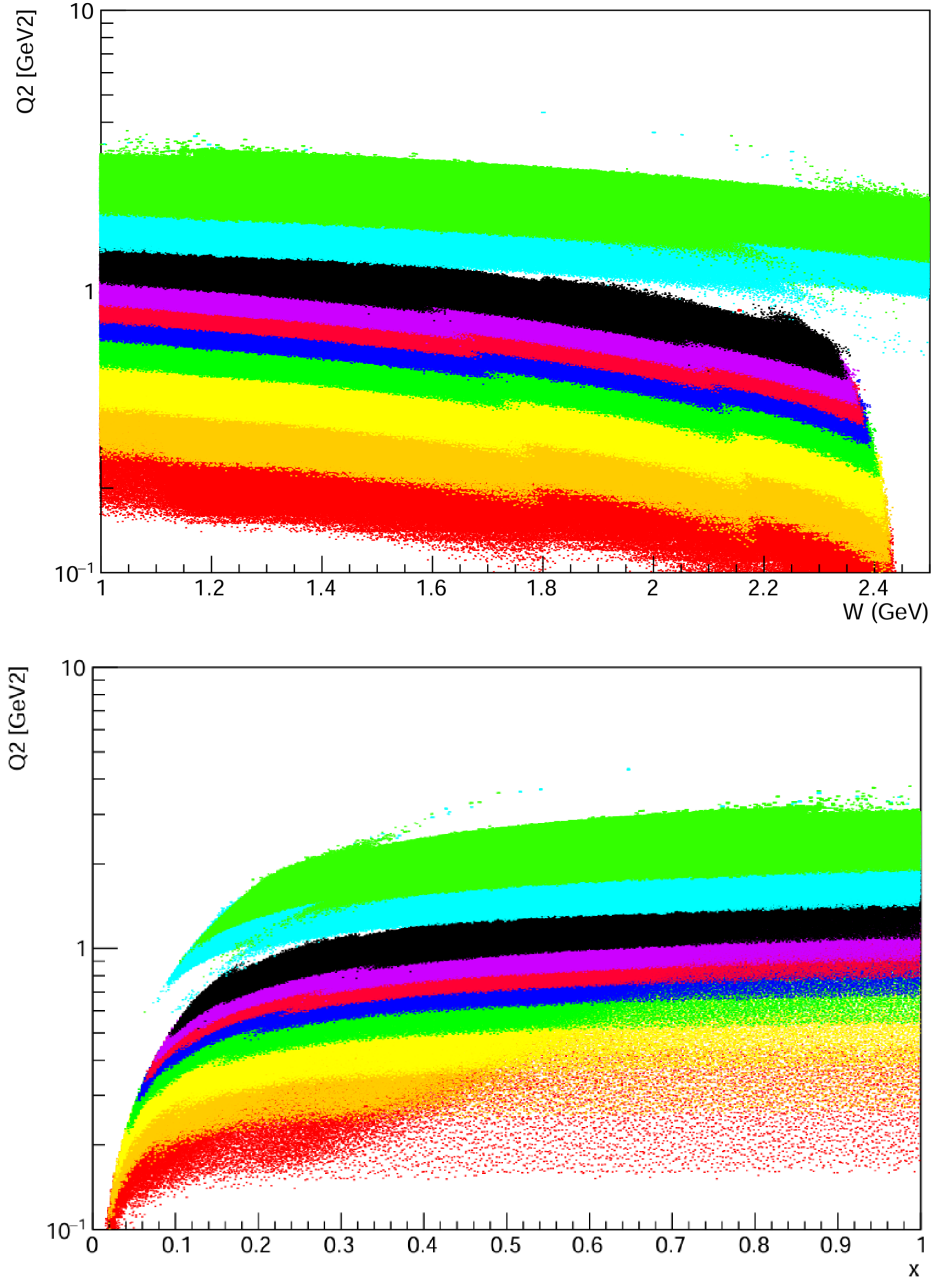


Figure 5: Kinematic coverage for the experiment proposed in this document. The red, orange, yellow, green, blue, pink, magenta, and black bands represent the 4.4 GeV data, from smallest scattering angle to largest. The cyan and green bands represent the 8.8 GeV data, from smallest scattering angle to largest. See Section 5 for specific angles and energy settings.

3.1 Required Equipment

This experiment will require the standard Hall C equipment package, with the addition of a polarized target and chicane magnets similar to what has been used for the previous g_2 measurements at Jefferson Lab. We will require the following technical support from JLab:

1. Installation of the target group's 5T polarized target.
2. Installation of an upstream chicane and associated support structures, following the design of [40].
3. Installation of the slow raster.
4. Operation of the beamline instrumentation for 50-100 nA beam.

We examine these requirements and other relevant instrumentation considerations in detail below.

3.1.1 Polarized Target

The polarized target has been successfully used in many experiments at Jefferson Lab, among the most recent are E01-006, E08-027, and E07-003. This target operates on the principle of Dynamic Nuclear Polarization, to enhance the low temperature (1 K), high magnetic field (5 T) polarization of solid materials (ammonia, lithium hydrides) by microwave pumping. The polarized target assembly contains several target cells of variable length (0.5-3.0 cm) that can be selected individually by remote control to be located in the uniform field region of a superconducting Helmholtz pair. The permeable target cells are immersed in a vessel filled with liquid Helium and maintained at 1 K by use of a high power evaporation refrigerator.

The target material is exposed to ≈ 140 GHz microwaves to drive the hyperfine transition which aligns the nucleon spins. The DNP technique produces proton polarizations of up to 90% in the NH_3 target. The heating of the target by the beam causes a drop of a few percent in the polarization, and the polarization slowly decreases with time due to radiation damage. Most of the radiation damage can be repaired by annealing the target at about 80 K, until the accumulated dose reached is greater than about $17 \times 10^{15} \text{ e}^-/\text{cm}^2$, at which time the target material needs to be replaced. The luminosity of the polarized material in the uniform field region is approximately $85 \times 10^{33} \text{ cm}^{-2} \text{ Hz}$.

The target will be operated with a magnetic field 90 degrees perpendicular to the beam at all times, to focus the collected data on σ_\perp . Several approved experiments are planning to use a similar polarized target in Hall C [41, 42], providing a possible opportunity for scheduling cooperation.

Operating the polarized target is a large task which will require dedicated work from our collaboration. However, previous experience with polarized target experiments at JLab [39, 8] indicates that graduate students were able to operate the polarized target and also fulfill numerous commitments to the experiment, with many of the target operators playing lead roles on the analysis. We believe we will be able to muster a multi-institutional work-force more than capable of meeting the needs of the polarized target alongside all the other work to be done on the experiment.

3.1.2 Chicane

To access g_2^p , the polarization direction will be held perpendicular to the beam axis for the majority of the experiment. This will create a non-negligible deflection of low energy electrons, so to ensure proper transport of the beam, a chicane will be employed. The first dipole will be located upstream of the target and gives the beam a kick out of the horizontal plane. The second dipole will be needed to be mounted on a stand with adjustable height over a range of around 85 cm, and is used to bend the beam back on the target with the required angle to compensate for the 5 Tesla field. Beam Position Monitors (BPMs) will be placed along the chicane line before and after each magnet to ensure proper transport of the beam. The deflection angles created by the 5T target field should be around 2.9 and 1.4 degrees for the 4.4 GeV and 8.8 GeV beam energies respectively.

Dr. Jay Benesch has designed a new chicane which should fulfill the requirements of compensation for the target field bending [40, 43]. Because of the small SHMS angles needed for the lowest 4.4 GeV settings, we will require the assistance of the lab staff and technicians in building and commissioning Dr. Benesch's new chicane design. This new chicane will locate the beam well within the profile of the target cell and the main hall beam dump [40], removing the need for a local dump as was used in

g2p [39] and SANE [21]. This new chicane is not a specialized piece of equipment only useful for this experiment. Rather, it may see significant future use, including in at least one other Hall C proposal currently submitting a Letter of Intent this year, possible future use with the SoLID detector in Hall A, and in any other experiment that needs to run with a non-longitudinal polarized target.

The lab technicians have expressed to us high confidence that this new system can be constructed in a timely manner and tested thoroughly. On the subject of the system's reliability, we defer to the judgement of the Jefferson Lab technicians and experts who have reviewed the design, and who have significant experience building and operating similar magnets. Dr. Jay Benesch, who designed the new chicane, is the longest serving member of the TAC and has designed resistive and superconducting magnets since 1976. He is confident that chicane design will work with high fidelity, that the existing electronics will be compatible, and that the diagnostic girder which will be used to house the chicane has been located [44].

Hall C Staff Scientist Dr. Dave Gaskell has communicated to us the following about the chicane: *"We have done this multiple times before. The process is relatively straightforward. ... We don't have any concerns that it can be done, but it will take some time so the work should begin well ahead of the expected installation and running [45]."* The collaboration plans to send a graduate student to assist the lab staff in building the chicane ahead of the experimental run.

The control software which will be used is standard, and refining the software will be part of the design and testing process for the chicane. According to Dr. Gaskell, *"The [chicane control software] will work."*

3.1.3 Raster

The existing Hall C fast raster will be used to generate a pattern up to 1 mm x 1 mm and will remain in its standard location [46]. The slow raster will be located approximately 10-12 meters upstream of the target, and can increase the final size up to a circular pattern with a 1 cm radius for 11 GeV [45], with a larger viable area for the requested energies of 8.8 and 4.4 GeV. The slow raster is necessary both for the large solid ammonia target that will be required, and to help mitigate the destruction of polarization by the beam discussed above.

3.1.4 Exit beam pipe and beam dump

A two inch beam pipe is sufficient to accommodate the rastered beam and expected multiple scattering. It is expected that a beam pipe extension will be necessary due to requiring the smallest angles available to the SHMS detector [46]. Due to the new chicane design discussed above [40], a local beam dump will not be necessary, and we will employ the main hall beam dump. This should keep the beam close enough to the central axis that a helium bag or other non-standard beam exit equipment should be unnecessary.

3.2 Beamline Instrumentation

We will require the standard equipment package of beamline instrumentation with no major modifications beyond that which is needed to install the chicane described above. The instrumentation needed for the experiment consists of Beam Current Monitors and Beam Position Monitors used to track the current and position of the electron beam, and polarimetry needed to determine the amount of beam electron polarization.

3.2.1 Beam Current and Beam Charge Monitor

Beam currents less than 100 nA are typically used with the polarized target in order to limit depolarizing effects and large variations in the density. Standard Beam Current Monitor(BCM) cavities have a linearity good to 0.2% for currents ranging from 180 down to 2 uA. Though it is possible that it will require further time to fully study the linearity, it is likely that the BCMs will remain linear down to 50 nA with the gain on BCM 1 and 2 switched to the highest setting [47].

3.2.2 Beam Polarimetry

We will utilize the Møller polarimeter as part of the standard Hall C equipment. During operation, 0.3 to 0.5 μA of current are incident on a foil of iron polarized by a magnetic field [46]. The expected systematic uncertainty [48, 45] of the Møller measurement is 2% or better. Møller runs will be scheduled at least once per energy change, and will be performed with the (non-chicaned) beam passing to the standard hall C dump.

The Compton polarimeter normally is used for a continuous non-invasive beam polarization monitor. However, it is not very well suited to run at low current, so the primary method of measuring the beam polarization will be with the Møller polarimeter.

3.2.3 The Spectrometers

For this experiment we will use only the SHMS detector, as the HMS detector is inappropriate at many of the scattering angles and energies requested. Performance of the spectrometers are well known so we can expect similar accuracies as for the GDH experiments on the polarized He3 target E94-010 and E97-110.

3.2.4 Detector Stack

The standard detector stack will be used for detecting electrons. We will require the usual horizontal drift chambers, hodoscope, the gas Cerenkov and lead glass shower calorimeter for particle identification. Since this is an inclusive measurement aiming only to measure scattered electrons, we will not require use of the Aerogel detector.

3.3 Synchrotron Radiation

Given the higher beam energy and target field angle compared to previous polarized target experiments in Hall C, it is necessary to consider the possibility of synchrotron radiation being significant enough to effect the rates. We estimate the heat load with a calculation of the power emitted by an electron beam in a dipole [49]:

$$P_e = 14.08 \frac{LIE^4}{\rho^2} \quad (13)$$

Where L is the length of the target field, I is the beam current, E is the beam energy, and ρ is the radius of curvature through the target field. Using Jay Benesch's simulations [43, 40] to estimate the radius of curvature, we obtain an approximate radiated power of around 0.019 W for the target field. Synchrotron radiation from upstream dipoles should be comparable in order of magnitude, or smaller, than this value. The new polarized target system is expected to have 1-3 W of cooling power, so we expect no issues with the synchrotron radiation damaging the target polarization.

3.4 Optics

It is likely that the optics changes introduced will be very similar to the previous polarized target experiments in Hall C such as SANE[21] and RSS[8]. According to Dave Gaskell[45], the optics changes are likely to be similar to what was seen for previous Hall C polarized target experiments. It has been previously possible to use the standard spectrometer optics in combination with a polarized target field map, and an iterative procedure to correct for the deflection [50]. This procedure involves beginning with the standard known SHMS optics and applying additional layers of reconstruction for the vertical beam offset and transportation through the target field. The vertical offset layer is constructed with slow raster position information, which is used to correct the focal plane quantities for the vertical shift. Transportation through the target field is treated through the use of a Runge-Kutta integration over a known target field map. This procedure will be iterated until the reconstructed beam position matches the information from the beam position monitors. To verify the optics are well understood, we will plan to take sieve slit data at each setting as a sanity check. This method should be less time consuming than a detailed optics study, and can even be started before the experiment actually runs. This will likely be a robust but highly doable project for a postdoc or senior graduate student.

3.5 Data Acquisition

We will utilize the standard Hall C data acquisition (DAQ) system which is based on CAEN V1190A TDC and FADC250 ADC. It is expected that the maximum allowed DAQ rate will be at least 40 kHz[51]. The calculated rates are on the order of 40 KHz or less, as seen in Section 5. It is therefore unlikely for us to be rate-limited or require a prescale factor.

3.6 Multiple Scattering

Last year there was a question in the ITAC report on if there could be a significant background from multiple scattering, due to the fact that the beam is rastered and the beamspot size can increase passing through the target. Without a target there is 6mm of clearance between the exit beampipe downstream of the target and the beam, so it is necessary to consider multiple scattering and determine the expected size of the beam as it exits the target.

We calculate the multiple scattering angle using [52]:

$$\theta_0 = \frac{13.6 \text{ MeV}}{p} z \sqrt{x/X_0} [1 + 0.038 \ln(x/X_0)] \quad (14)$$

Here, p is the smallest momentum of the proposal, 4.4 GeV. z is the charge number (1) of an electron. $\frac{x}{X_0}$ is the number of radiation thicknesses passed through, for which we assume similar numbers as were investigated in the E08-027 target [53]. With these numbers we obtain an estimated $\theta_0 = 0.027^\circ$. The multiple scattering spreads the rastered beam spot into a gaussian distribution, where 98% of the electrons will fall within one θ_0 of their initial trajectory. Taking information from the comment, we calculate the length needed for the beam to expand 6 mm with:

$$L = \frac{6 \text{ mm}}{\tan \theta_0} = 12.684 \text{ m} \quad (15)$$

Based on the drawings we have received of the small-angle beampipe, the first two small sections of beam extend around 3.302 meters from the target chamber, after which the beam pipe expands to a larger size. Considering the above multiple scattering calculation, the beam should easily clear this distance without using up the 6 mm clearance. The angle to hit the beampipe (6 mm expansion) within this 3.302 meter section turns out to be around $3.8 \theta_0$. Consequently, the amount of beam current which may interact with the pipe should be less than 0.0008% of the beam. Accordingly, we do not anticipate multiple scattering will create a problematically large beam spot.

3.7 Low-x Contributions

Without full coverage in x from the pion production threshold to $x = 0$, it is of course impossible for any experiment to measure the full integral for the moments described in this document. As doing so would require collecting data to an infinite invariant mass W , it is only practically possible only to measure truncated moments over a limited x range. There is a long and successful history of prior experiments measuring these truncated moments out to a similar W -range as is proposed in this document [39, 11, 21, 10, 25, 8], using various techniques to estimate the total integral. A natural question then is if the coverage obtained by this proposal is sufficient to draw any conclusions about these moments. As it is possible for the Hall C spectrometers to measure very close to the pion production threshold, the high- x part of the integral is not a concern, and we need only consider how to form moments including the missing low- x part. For \bar{d}_2 , we are largely shielded from the impact of the unmeasured low- x region by the kinematic weighting of the integral. This is straightforwardly evident for most settings if we examine a running integral of the model predictions from the CLAS Hall B model for this moment, as shown in Figure 6.

This figure indicates that by the lowest x expected for all of the settings, the integral is expected to have saturated, with the obtained data accounting for nearly 100% of the integral. The only point expected not to be fully saturated is the highest Q^2 8.8 GeV setting, the data for which will still covers almost 80% of the expected value of the integral. A very reasonable estimate of the total integral can then be obtained by using a model-driven procedure to fill in the small missing part of the integral, with a corresponding increase to the systematics of that setting. This procedure has been used in the past, and will not be a dominating systematic error for the relevant setting.

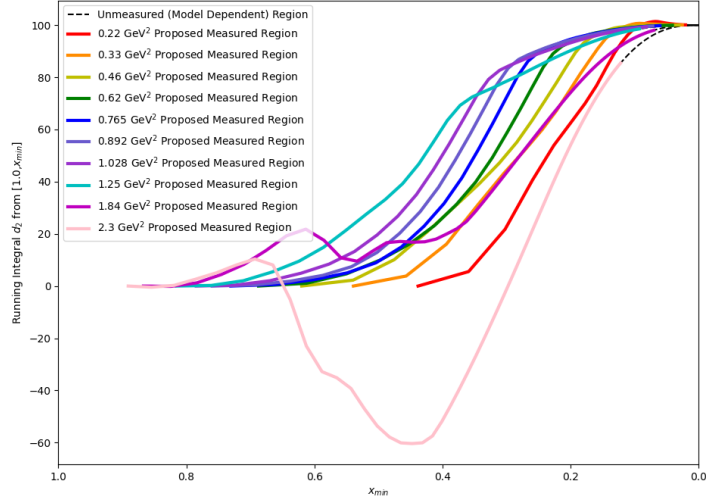


Figure 6: Running integral of $\overline{d_2}$ from high Bjorken- x on the left to low x on the right, calculated with the CLAS Hall B Model [10]. The colored lines represent the measured region for each kinematic setting, while the black dashed lines indicate the expected contribution of the unmeasured region. The y-axis indicates percentage of the total d_2 integral which has been obtained when integrating from $x = 1$ to the value on the x-axis. All settings except the highest Q^2 point are expected to converge essentially to 100% of the integral due to the integrand's weighting towards high Bjorken- x .

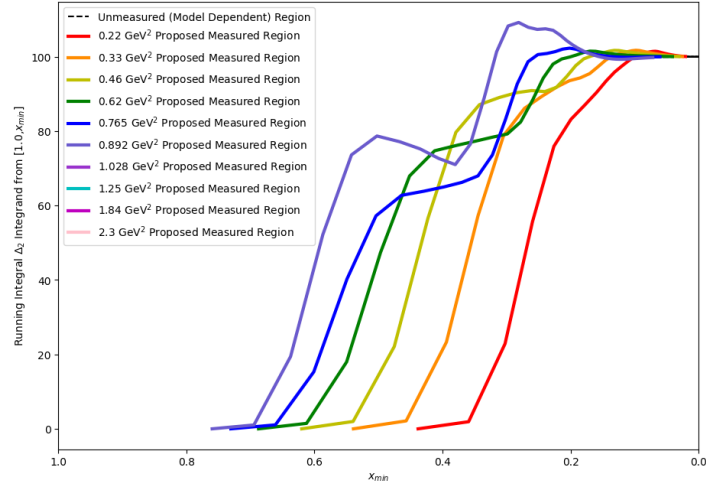


Figure 7: Running integral of Δ_2 in electronic hydrogen from high Bjorken- x on the left to low x on the right, calculated with the CLAS Hall B Model [10]. The colored lines represent the measured region for each kinematic setting, while the black dashed lines indicate the expected contribution of the unmeasured region. The y-axis indicates percentage of the total d_2 integral which has been obtained when integrating from $x = 1$ to the value on the x-axis. All settings are expected to converge essentially to 100% of the integral due to the integrand's weighting towards high Bjorken- x . The two 8.8 GeV beam settings are not relevant to this moment.

Similar behaviour is seen for the hydrogen hyperfine contribution Δ_2 in Figure 7. Because of the kinematic weighting, the Δ_2 integrand should be more than 96% saturated for all of the kinematic settings in a relevant Q^2 range.

One other method by which we plan to try and understand the low- x region is by extracting g_2 's first moment, Γ_2 , which is absent the Bjorken- x weighting which makes an approximation of the full moment possible for \overline{d}_2 and Δ_2 . The unsubtracted dispersion relations for the covariant spin-dependent doubly-virtual Compton scattering (VVCS) amplitudes S_2 and νS_2 lead to a super-convergence relation for Γ_2 based on Regge asymptotics which is valid for all Q^2 :

$$\Gamma_2 = \int_0^1 g_2(x, Q^2) dx = 0, \quad (16)$$

where the integration includes the elastic peak. This sum rule was originally proposed by Burkhardt and Cottingham and is known the Burkhardt-Cottingham or B.C. Sum Rule [54]. At first glance, it appears to be a trivial consequence of the $n = 1$ term of the operator product expansion (OPE) of Γ_2 (See for example [55]). But the expansion is valid only for $n \geq 3$. The OPE actually gives no information about the BC sum rule [3].

Though the fulfillment of the B.C. Sum Rule is currently still something of an open question, all existing data is in good agreement with the sum rule's requirement for g_2 to integrate to zero over x , at all Q^2 . If we assume continued fulfillment of the B.C. sum rule, the amount which our Γ_2 result differs from 0 can be used to constrain the low- x part of the g_2 part of the integral for \overline{d}_2 and other moments. Further, as was discussed previously, it may be possible to employ quark helicity evolutions to low- x , similar to techniques used for g_1 on $g_T = g_1 + g_2$. The data for the proposed experiment will aid in the construction of these evolutions, and once complete, they may be applied to generate a proper test of the B.C. sum rule for this and other low Q^2 g_2^p results.

For these reasons, we believe the proposed data will be sufficient to estimate the full value of \overline{d}_2 and Δ_2 with high precision, and provide useful results which aid in obtaining a better understanding of the higher twist behaviour of Γ_2 and other moments. These techniques have been tested and proven successful by a suite of other Jefferson Lab experiments which measured truncated moments and have driven new advances in our knowledge of nucleon spin structure [39, 8, 21, 11, 10].

3.8 Statistics and Systematics

Based on the calculated rates, the beamtime request is chosen to keep the statistical error on \overline{d}_2 less than 5% for all the 4.4 GeV beam kinematic settings, and less than 8% for both of the 8.8 GeV beam kinematic settings. Because the rates fall as Q^2 increases, it is more difficult to get small statistical uncertainty at higher Q^2 , but the time requested is more than sufficient for a significant improvement in statistical precision over previous g_2 measurements at Q^2 above and below the planned regime.

With regard to the systematics, we have a strong historical guide on what to expect: several JLab experiments have performed measurements similar to what we propose here (for example, see Refs. [56, 8, 57, 38, 21, 39]). From these previous endeavors, we can make an estimate of the systematic uncertainty. Table 1 gives an estimate of the most significant sources of error, while Table 2 gives further detail on the contributions to the cross section uncertainty which will be the dominant error. Previous experience with similar measurements [56] has shown that we can obtain 4-5% systematic uncertainty [58, 59, 60] on cross section measurements, with the largest uncertainty (2-3%) coming from the knowledge of the acceptance.

Figs. 8 to 12 show the projected accuracy we can obtain with the below beam time request of 26 PAC Days. The systematic error bands on the axes for the moment results represent the total from Table 1. The projected uncertainties have been evaluated assuming the central values predicted by the Hall B model [10]. We plan to publish results for each of g_2 's moments for all 10 Q^2 points shown with the high precision displayed on the following plots. We will also publish results for the g_2 spectrum binned in x and Q^2 , as well as Wandzura-Wilczek subtracted results in the form of \overline{g}_2 to study the twist-3 contributions. Projected results for these structure function spectra are shown below.

The following plots are produced using the Hall B model [10] for the central value, and with 30 MeV binning. A larger binning at high W similar to that employed by previous experiments [39, 11] may reduce the error bars shown on these plots in exchange for a larger resolution. The error on \overline{g}_2 is estimated using our expected g_2 statistics and systematics, combined with the statistics and

Source	(%)
Cross section	5-7
Target Polarization	3.0
Beam Polarization	3.0
Radiative Corrections	3.0
Parallel Contribution	2.0
Const. Q^2 Adjustment	≤ 1
Total	7.5-8.9

Table 1: Total Systematic Uncertainties.

Source	(%)
Acceptance	4-6
Packing fraction	3.0
Charge determination	1.0
VDC efficiency	1.0
PID detector efficiencies	≤ 1
Software cut efficiency	≤ 1
Energy	0.5
Resolution Bin-Migration	≤ 2
Deadtime	≤ 1
Total	5-7

Table 2: Major contributions to the cross section systematic of Table 1.

systematics from the EG4 and EG1b experiments' results [11, 10] used for the g_1 contribution to g_2^{ww} at compatible kinematics.

3.9 Kinematics

The spectrometer configurations, with associated running time, are summarized in Table 3. The sixth column represents the rate (in each bin) from the proton, while the seventh shows the total prescaled rate seen by the spectrometer. The calculation of these rates, along with more details on the requested beam time is detailed in Section 6. These settings are chosen to cover the resonance region from a minimum W of the pion production threshold ($W=1.07$ GeV) to a maximum W of at least 2.0 GeV. They are also selected to provide 10 separate Q^2 settings, 8 settings covering the gap between the g2p and RSS experiments, and 2 settings covering the gap between the RSS and SANE experiments. A target cell packing fraction of 0.55 is assumed.

Table 3: Kinematic Settings.

E_0	Θ	P_0	W	Q^2	Rate P (Hz)	Rate (kHz)	Pre	\mathcal{L}	$P_b P_t$	I (nA)	Time (h)
4.4	6.5	3.607	1.47	0.204	77	39.9	1	0.9E+35	0.60	85	1.0
4.4	6.5	2.661	2.00	0.151	65	25.1	1	0.9E+35	0.60	85	1.0
4.4	6.5	1.963	2.31	0.111	69	18.9	1	0.9E+35	0.60	85	1.0
0.1 PAC days											
4.4	8.0	3.607	1.44	0.309	41	21.4	1	0.9E+35	0.56	85	1.3
4.4	8.0	2.661	1.98	0.228	28	11.5	1	0.9E+35	0.56	85	1.9
4.4	8.0	1.963	2.30	0.168	30	8.3	1	0.9E+35	0.56	85	1.8
0.2 PAC days											

continued on next page

Table 3: Kinematic Settings.

E_0	Θ	P_0	W	Q^2	Rate P (Hz)	Rate (kHz)	Pre	\mathcal{L}	$P_b P_t$	I (nA)	Time (h)
4.4	9.5	3.607	1.39	0.435	18	9.1	1	0.9E+35	0.60	85	2.3
4.4	9.5	2.661	1.96	0.321	14	5.9	1	0.9E+35	0.60	85	3.0
4.4	9.5	1.963	2.28	0.237	15	4.3	1	0.9E+35	0.60	85	2.8
0.3 PAC days											
4.4	11.2	3.607	1.33	0.610	7	3.7	1	0.9E+35	0.56	85	6.0
4.4	11.2	2.661	1.92	0.450	6	3.0	1	0.9E+35	0.56	85	6.5
4.4	11.2	1.963	2.26	0.332	7	2.2	1	0.9E+35	0.56	85	5.9
0.8 PAC days											
4.4	12.5	3.607	1.27	0.752	4	2.0	1	0.9E+35	0.57	85	9.1
4.4	12.5	2.661	1.89	0.555	4	1.9	1	0.9E+35	0.57	85	8.5
4.4	12.5	1.963	2.25	0.409	4	1.5	1	0.9E+35	0.57	85	7.6
1.1 PAC days											
4.4	13.5	3.607	1.22	0.877	2	1.3	1	0.9E+35	0.56	85	16.5
4.4	13.5	2.661	1.87	0.647	3	1.3	1	0.9E+35	0.56	85	13.7
4.4	13.5	1.963	2.23	0.477	3	1.1	1	0.9E+35	0.56	85	12.1
1.8 PAC days											
4.4	14.5	3.607	1.17	1.011	1	0.8	1	0.9E+35	0.56	85	23.2
4.4	14.5	2.661	1.84	0.746	2	1.0	1	0.9E+35	0.56	85	17.4
4.4	14.5	1.963	2.21	0.550	2	0.8	1	0.9E+35	0.56	85	14.9
2.3 PAC days											
4.4	16.0	3.607	1.07	1.229	0	0.4	1	0.9E+35	0.56	85	50.8
4.4	16.0	2.661	1.80	0.907	1	0.6	1	0.9E+35	0.56	85	32.7
4.4	16.0	1.963	2.19	0.669	1	0.5	1	0.9E+35	0.56	85	26.6
4.6 PAC days											
8.8	9.5	7.213	1.46	1.741	1	1.3	1	0.9E+35	0.56	85	12.9
8.8	9.5	5.321	2.47	1.284	1	1.6	1	0.9E+35	0.56	85	9.3
0.9 PAC days											
8.8	11.0	7.213	1.24	2.332	0	0.5	1	0.9E+35	0.56	85	14.3
8.8	11.0	5.321	2.38	1.721	0	0.8	1	0.9E+35	0.56	85	8.2
0.9 PAC days											

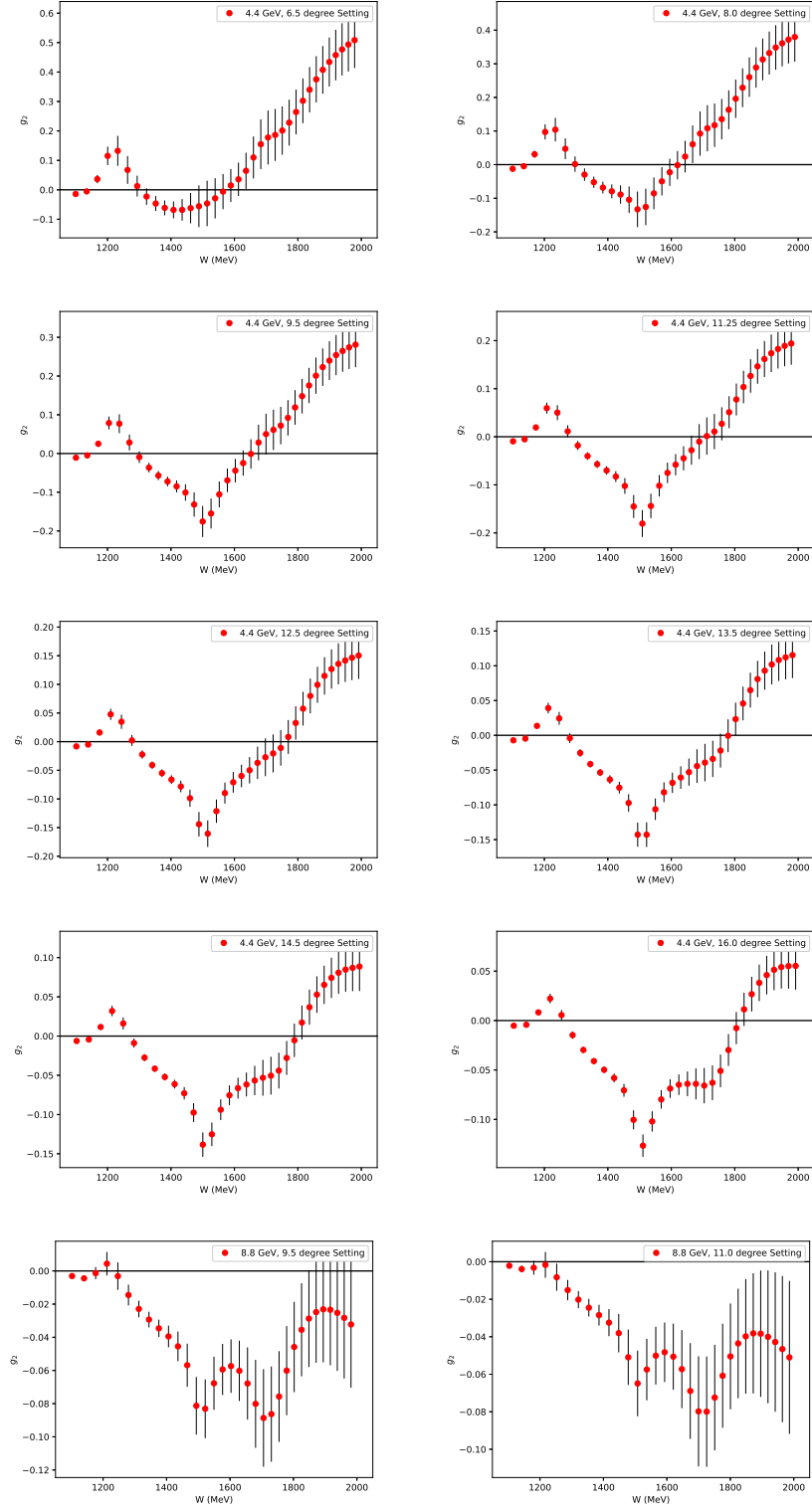


Figure 8: Projected g_2 Spectra with 30 MeV binning.

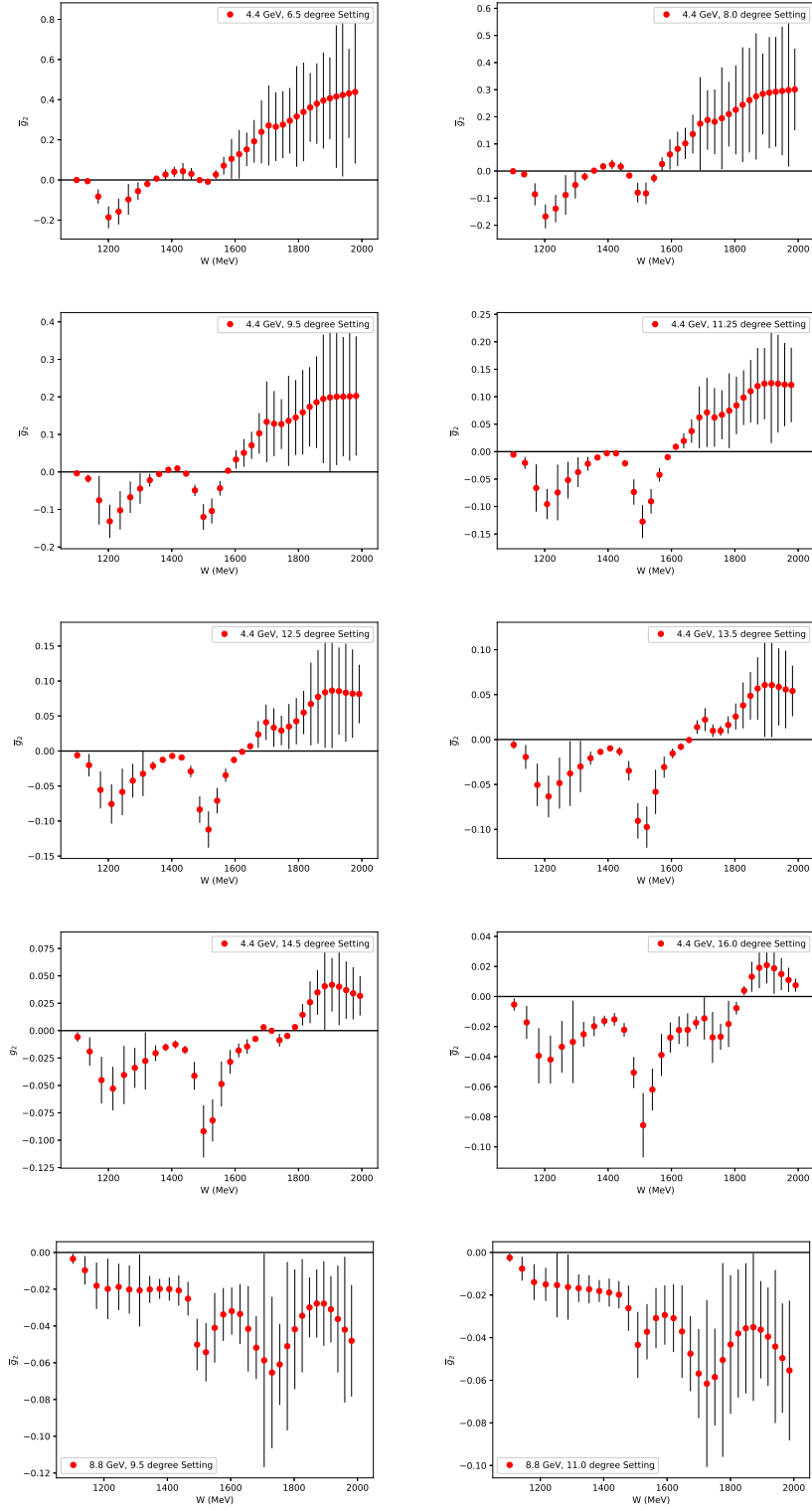


Figure 9: Projected \bar{g}_2 Spectra with 30 MeV binning.

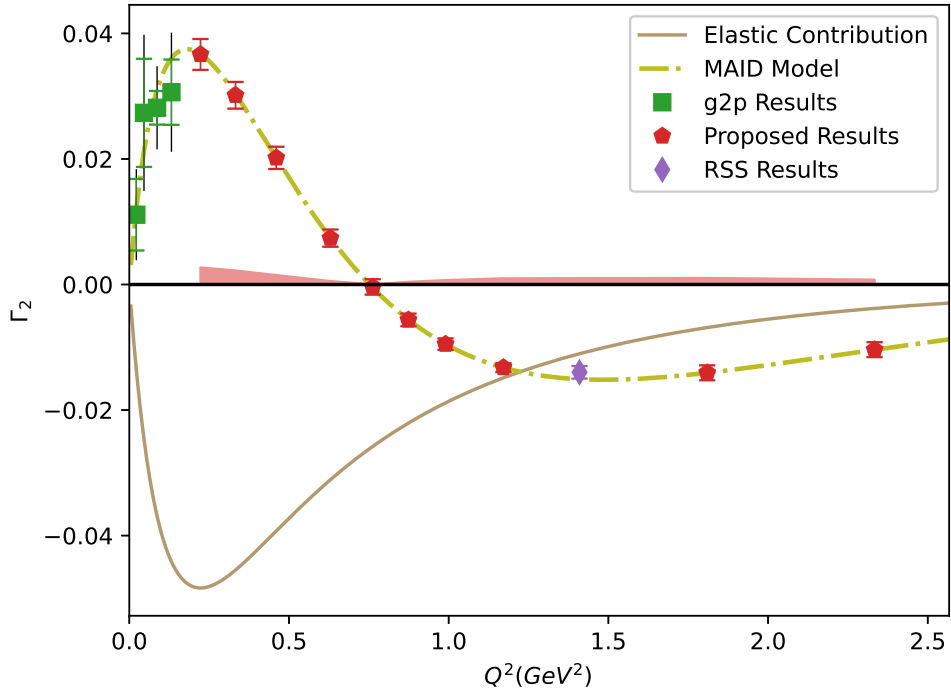


Figure 10: Projected results for Γ_2^p . Data shown is estimated over the resonance region. Statistical errors are shown on the symbols. Systematic for measured region is represented by the light band. Uncertainties for the measured region are evaluated assuming the central value predicted by the Hall B [10] model. Elastic curve is from Ref. [61].

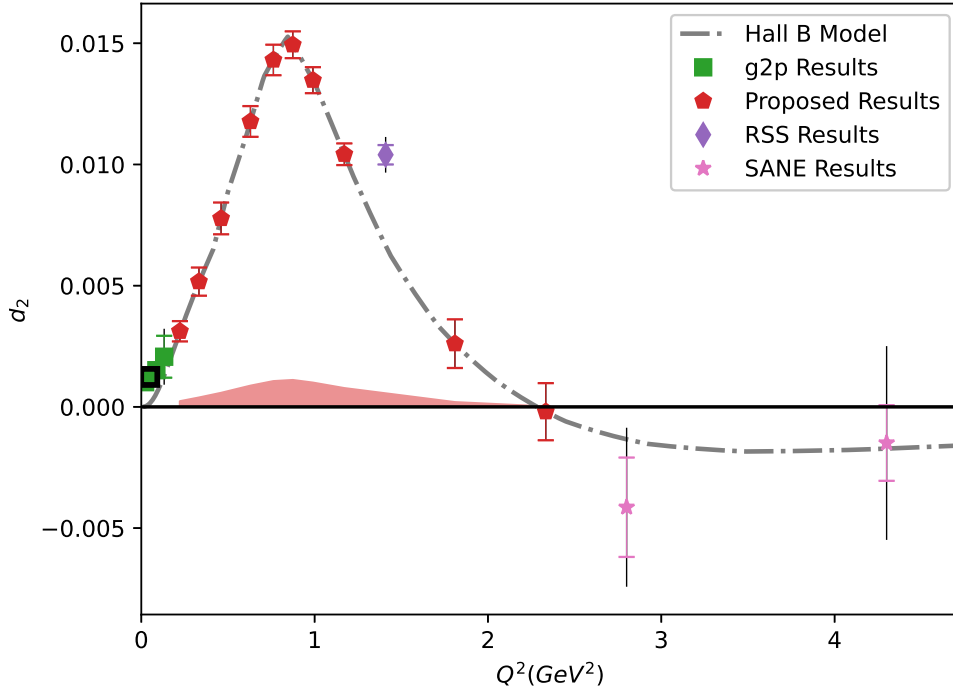


Figure 11: Projected results for d_2^p . Statistical errors are shown on the symbols. Systematic is represented by the band on the axis. Uncertainties are evaluated assuming the central value predicted by the Hall B [10] model. The inner (outer) band represents statistical (systematic) uncertainty. Unmeasured non-resonance contribution is highly suppressed by x^2 weighting of d_2 and is not shown.

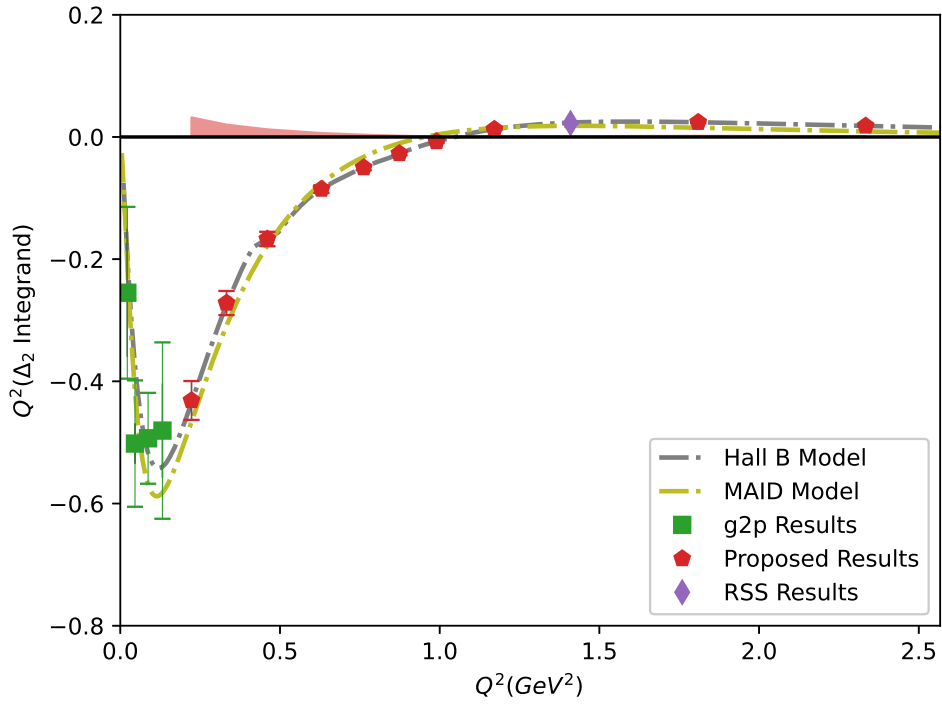


Figure 12: Projected results for the Δ_2 hyperfine structure contribution for muonic hydrogen. Statistical errors are shown on the symbols. Systematic is represented by the band on the axis. Uncertainties are evaluated assuming the central value predicted by the Hall B [10] model.

4 Analysis Method

The extraction of the g_2 structure function from polarized proton data is at this point a well studied process from previous JLab experiments [39, 8, 21]. We will rely on expertise carried over from those previous experiments to streamline the analysis process, which will utilize a measurement of the polarized cross section differences in order to determine the spin structure function g_2^p . These quantities are defined as the difference between the cross section for forward and backward helicity electron scattering with a polarized target. We can define two polarized cross section differences in a simple way, one for a target polarized longitudinally to the electron beam, and another for a target polarized transverse to the electron beam [62]:

$$\Delta\sigma_{\parallel} = 2A_{\parallel}\sigma_0 \quad (17)$$

$$\Delta\sigma_{\perp} = 2A_{\perp}\sigma_0 \quad (18)$$

Here, $A_{\parallel(\perp)}$ is the longitudinal (transverse) helicity asymmetry, and σ_0 is the unpolarized cross section. For this experiment, we will be measuring both σ_0 , the standard experimental cross section, and A_{\perp} , defined as:

$$A_{\perp} = \frac{\sigma_{+}^{\perp} - \sigma_{-}^{\perp}}{\sigma_{+}^{\perp} + \sigma_{-}^{\perp}} \quad (19)$$

Where σ_{+} and σ_{-} represent the cross sections for forward and backward helicity scattering electrons, respectively, both with a transversely polarized proton target. Because the asymmetry is a ratio of cross sections, many scaling factors in the experimental cross section cancel. This makes the asymmetry easier to measure than the cross section because many possible systematic sources, such as the detector acceptance, will cancel out. We intend to also extract the standard unpolarized experimental cross section σ_0 directly to form $\Delta\sigma_{\perp}$ as defined above. However, there is a significant amount of world data on unpolarized proton scattering over a broad kinematic range, meaning that in the case of large cross section systematics, a viable option would be to use world data or a model input for the unpolarized part, as was done in the analysis of E08-027 [39].

4.1 Extraction of the g_2 Structure Function

The spin structure functions are related to the spin-dependent cross sections via [62, 63]:

$$\begin{aligned} g_1 &= \frac{MQ^2}{4\alpha_e^2} \frac{y}{(1-y)(2-y)} \left[\Delta\sigma_{\parallel} + \tan \frac{\theta}{2} \Delta\sigma_{\perp} \right] \\ g_2 &= \frac{MQ^2}{4\alpha_e^2} \frac{y^2}{2(1-y)(2-y)} \left[-\Delta\sigma_{\parallel} + \frac{1 + (1-y) \cos \theta}{(1-y) \sin \theta} \Delta\sigma_{\perp} \right] \end{aligned} \quad (20)$$

where $y = \nu/E$.

Here, the polarized cross section differences are represented by $\Delta\sigma_{\parallel}$ and $\Delta\sigma_{\perp}$. Measuring polarized cross section differences results in the cancellation of the contribution from any unpolarized target material and obviates the need for any external model input. This formulation of the structure functions does not include target mass corrections. We plan to investigate the target mass corrections separately through the use of Nachtmann moments and the methodology of Y.B. Dong [64], and contrast to the Cornwall-Norton moments defined earlier in this document. As an example of the estimated scale of the target mass corrections, see Figure 13 below, which shows the ratio of target mass corrected $2M_2^{(3)}$ to the standard Cornwall-Norton moment \bar{d}_2 . This figure shows that the target mass corrected Nachtmann moment varies from around 70-80% of the Cornwall-Norton moment. The target mass corrections are most relevant in the twist-3 regime, near the higher kinematics of this proposal. We will publish both target mass corrected Nachtmann moment results as well as our raw results, to enable theorists wishing to compare to our data to treat the target mass corrections in a different way if they desire.

We can recast Eq. 20 in the form:

$$\begin{aligned} g_1 &= K_1(a_1\Delta\sigma_{\parallel} + b_1\Delta\sigma_{\perp}) \\ g_2 &= K_2(c_1\Delta\sigma_{\parallel} + d_1\Delta\sigma_{\perp}) \end{aligned} \quad (21)$$

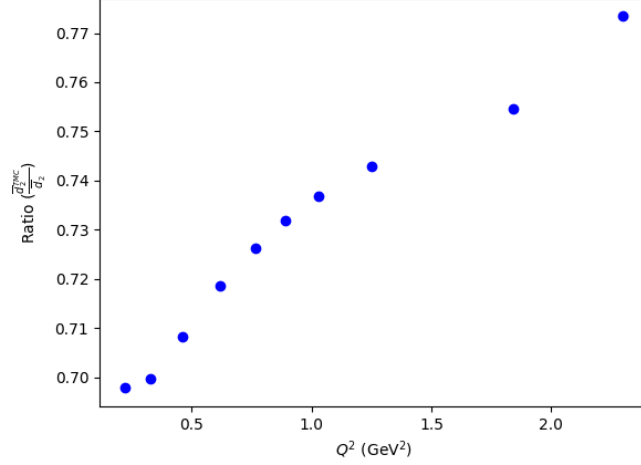


Figure 13: The ratio of target mass corrected Nachtmann moment $2M_2^{(3)}$ [64] to the Cornwall-Norton moment \bar{d}_2 with no mass corrections, for each of the kinematic settings of PR12-24-002. The Nachtmann moment is calculated using the methodology of Y.B. Dong [64] for the kinematics of each fixed Q^2 setting of this proposal. This Nachtmann moment is then divided by the Cornwall-Norton moment $\bar{d}_2 = \int x^2 (2g_1(x, Q^2) + 3g_2(x, Q^2)) dx$ to obtain the values shown in the plot.

where

$$\begin{aligned}
K_1 &= \frac{MQ^2}{4\alpha_e^2} \frac{y}{(1-y)(2-y)} \\
K_2 &= \frac{MQ^2}{4\alpha_e^2} \frac{y^2}{2(1-y)(2-y)} = K_1 \frac{y}{2} \\
a_1 &= 1 \\
b_1 &= \tan \frac{\theta}{2} \\
c_1 &= -1 \\
d_1 &= \frac{1 + (1-y) \cos \theta}{(1-y) \sin \theta}
\end{aligned}$$

Equation 21 reveals that the parallel contribution to g_2 is highly suppressed (See Fig. 14). In fact, the relative weight of the $\Delta\sigma_{\parallel}$ contribution to g_2 ranges from 2 to 12% for all proposed kinematics. Since our proposed experiment will not measure $\Delta\sigma_{\parallel}$, we will use the high precision data from Hall B experiments EG4 [11] and EG1b [34], which reported an average uncertainty of approximately 10%. Given the ratio of $|c_1/d_1|$ shown in Figure 21, this leads to around a 2% or less error contribution to our g_2 for all kinematics.

In practice, the Hall B cross section data is not at the exact same kinematics as our proposal, which makes it difficult to directly combine the respective cross sections. Instead, we will use the EG4 and EG1b g_1 data, which has been shown in the previous analysis of E08-027 to be easily adjusted to nearby constant Q^2 with minimal impact on the central value of the structure function [39]. Inverting Eq. 20 yields:

$$\begin{aligned}
\Delta\sigma_{\parallel} &= \frac{4\alpha_e^2}{MQ^2} \frac{(1-y)(2-y)}{y} \left(\frac{2}{y} \right) \frac{\frac{1+(1-y)\cos\theta}{(1-y)\sin\theta} \frac{y}{2} g_1 - \tan\theta/2 g_2}{\frac{1+(1-y)\cos\theta}{(1-y)\sin\theta} + \tan\theta/2} \\
\Delta\sigma_{\perp} &= \frac{4\alpha_e^2}{MQ^2} \frac{(1-y)(2-y)}{y} \left(\frac{2}{y} \right) \frac{\frac{2}{y} g_1 + g_2}{\frac{1+(1-y)\cos\theta}{(1-y)\sin\theta} + \tan\theta/2}
\end{aligned} \tag{22}$$

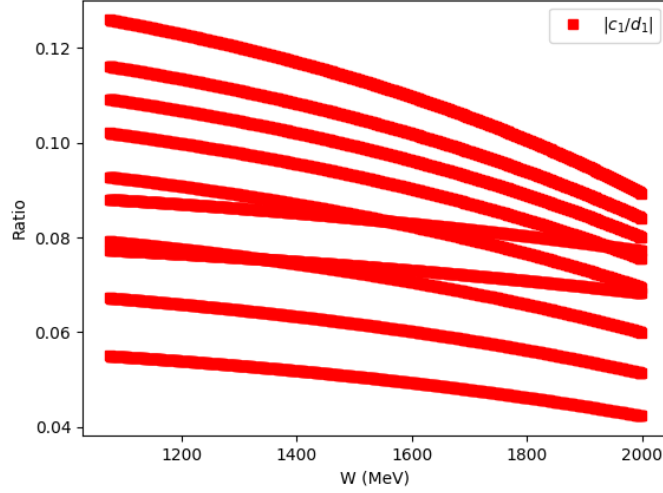


Figure 14: Relative weighting of the $\Delta\sigma_{||}$ contribution to g_2 . See Eq. 21.

Eq. 22 can be recast in the form:

$$\Delta\sigma_{||} = K_3(a_2g_1 + b_2g_2) \quad (23)$$

$$\Delta\sigma_{\perp} = K_4(c_2g_1 + d_2g_2) \quad (24)$$

where

$$\begin{aligned} K_3 &= \frac{4\alpha_e^2}{MQ^2} \frac{(1-y)(2-y)}{y} \left(\frac{2}{y}\right) \frac{1}{a_2 - b_2} \\ K_4 &= \frac{4\alpha_e^2}{MQ^2} \frac{(1-y)(2-y)}{y} \left(\frac{2}{y}\right) \frac{1}{a_2 - b_2} \\ a_2 &= \frac{1 + (1-y)\cos\theta}{(1-y)\sin\theta} \frac{y}{2} \\ b_2 &= -\tan\theta/2 \\ c_2 &= \frac{2}{y} \\ d_2 &= 1 \end{aligned}$$

So in terms of the existing Hall B g_1 and the measured $\Delta\sigma_{\perp}$, g_2 can be expressed:

$$g_2 = \left(\frac{1}{1 - K_2K_3c_1b_2} \right) [d_1\Delta\sigma_{\perp} + K_2K_3c_1a_2 g_1] \quad (25)$$

4.2 Interpolation to Constant Q^2

The data measured at constant incident energy and scattering angle will be interpolated¹ to a single constant Q^2 for each of the 10 kinematic settings of this proposal. This is necessary to perform an integration over x at constant Q^2 to obtain values for the moments \bar{d}_2 , Γ_2 , and the hyperfine splitting contribution. The good kinematic coverage and overlap should facilitate a straight forward interpolation.

For each kinematic setting, we choose the constant Q^2 to be the Q^2 associated with the data at the peak of the $\Delta(1232)$ resonance. We then use a model-driven procedure, in which we compute the g_2

¹as has been done in experiments E08027, E94010, E97110 and E01012.

value output by a phenomenological model at each W point of the result. We check the model output for the arbitrary Q^2 that each bin lands at, and for the chosen constant Q^2 of the setting. We then apply the additive difference between these two model results as a correction to each point on the W spectrum of g_2 .

$$\Delta g_2^{corr} = g_2^{model}(x, Q_{const}^2) - g_2^{model}(x, Q^2) \quad (26)$$

$$g_2(x, Q_{const}^2) = g_2(x, Q^2) + \Delta g_2^{corr} \quad (27)$$

It was shown in E08-027 [39] that this method works well when driven by the Hall B Model [34]. This scaling factor has been shown at the kinematics of E08-027 to contribute only small adjustments to the structure function, on the order of 1% or less. Given that the settings proposed for this experiment have far less Q^2 variation than E08-027 as seen in Figure 5, it is likely that the constant Q^2 interpolation will prove to be negligible.

5 Simulation Results

The report from PAC-52 stated just one major issue with the previous iteration of this proposal: ‘*The impact of this new setup on the detector resolution and its subsequent effect on the physics results has not been thoroughly addressed. A full Monte Carlo simulation of the new setup and detector is needed.*’ The collaboration recognizes the salient nature of this request and has invested significant time in fulfilling it by studying and following the simulation procedure used for all other small-acceptance spectrometer experiments in Hall C and Hall A. Below, we discuss the general simulation procedure used in these halls, and the results from our simulation of this experiment.

5.1 Hall A/C Simulation Procedures & Simulation Details

The simulation needs of a small-acceptance spectrometer such as the SHMS used in this proposal are very different from those of a large-acceptance detector such as the ones used at CERN, BNL, and in Hall B, in large part because of a much smaller background contribution. The spectrometers in Hall A and C have around a 4 msr acceptance and are extensively shielded, meaning the background is very small [46]. The general simulation package used in Hall A and C for previous experiments with and without polarized targets consists of a Monte-Carlo simulation in which particles are generated over a limited phase space and projected through the detector geometry [65]. Magnetic elements are simulated using COSY, a code for magnetic optics transport designed at Michigan State University [66] which uses a matrix for transport through each magnetic element. Transport through the polarized target field is performed using a target field map and Runge-Kutta method, along with an iterative procedure to obtain the reconstructed momentum [45]. In contrast with tools like Pythia that are used for the large-acceptance spectrometers where the background contribution is large, the Hall C Monte-Carlo simulates specifically the small class of processes that dominate at these kinematics. The Hall C simulation package branches into two tools, SIMC, which is used for coincidence, and MC-Single-Arm, which is used for inclusive experiments and includes precision information about the HMS and SHMS detectors, including real apertures, fiducial cuts for detectors, sequential transformations for magnetic elements and continuous drift in field-free regions.

We have employed a variant on this standard Hall C simulation, which includes models for radiative effects, multiple scattering, ionization energy loss, particle decay, and other effects. It also includes a track reconstruction procedure, which uses the smeared position at the drift chamber to fit the track at the focal plane, and then reconstructs to the target using matrix elements fit from Monte-Carlo data [65]. D. Gaskell maintains a version of this standard simulation which includes a model for transport through a polarized target field, which we have employed and will be discussed below.

The effects of the new chicane dipoles on the beam are currently modeled using a Bmad model performed by Ryan Bodenstein based on initial work done by Jay Benesch [40, 67]. This simulation uses a Runge-Kutta method to optimize the transport of the beam through the chicane and target field, and, along with preliminary work done in OptiM by Dr. Benesch, provides us with the impact of the chicane on the beam particles, which we apply to the Monte-Carlo generated particles entering the target field.

The impact of the target field is then handled using COSY and a target field map of the 5T transverse target field, also provided by Dr. Benesch. The target field is used to transport the

trajectory up to the first detector magnetic element, at which point the COSY matrix element for the first detector magnet is used. A Runge-Kutta method is used to step the particle through the magnetic field, such that the transport of the particle is handled fairly simply with a transport matrix and ray tracing. Less simple is the reconstruction employed to obtain the kinematics at the target center [45]. A single reconstruction matrix is used, which gives reconstructed quantities at $z = 0$ in the spectrometer coordinate system. In the presence of a target field, this will initially be an incorrect reconstruction of the kinematics at the target, due to the out-of-plane contribution on the beam at the target. An iterative approach is used to correct this. The vertical position of the beam from the raster is used to get a first order reconstruction at $z = 0$; Those initially incorrect values are projected out of the field region and then swum back to the target using the Runge-Kutta procedure. This will alter the values for the kinematic quantities δp and the in and out of plane scattering angles, but it will also yield a new value for the vertical position of the beam, which can be used to restart the procedure. This procedure is iterated until the vertical position of the beam converges [45].

Finally, the simulated particles with the kinematic changes introduced by the chicane and target field are stepped through the detector geometry and the resulting measured kinematics are reconstructed back to the target. To study the resolution as charged by PAC-52, we need to compare the generated Monte-Carlo particles to the reconstructed quantities and investigate the resulting resolutions for the momentum and scattering angles. For the experiment to be feasible, the size of these resolutions should be smaller than the needed bin size for each kinematic quantity, and we should be able to correct for any failing of the reconstruction without introducing a large new systematic error that would impact our overall systematic.

5.2 Simulation Output

We have studied the results of the simulation for all 28 kinematic settings of this proposal. Below, we show the results of the “worst case” kinematic setting, with beam energy $E=4.4$ GeV, Detector central momentum $p = 3.607$ GeV, and central scattering angle $\theta = 6.5^\circ$. The other kinematic settings are either comparable or show less impact of the transverse target field and chicane than the plots shown here. The $E=8.8$ GeV settings in particular see practically no effect, because the deflection from the target field is much smaller.

The kinematic quantities δp , θ , and ϕ , representing the scattered momentum, in-plane scattering angle, and out-of-plane scattering angle respectively, are shown in Figs 15- 17 with and without the target field and chicane accounted for. As we can see, the most significant impact from the target field is on the out-of-plane scattering angle ϕ . This is consistent with the data from previous similar experiments, which also had a large out-of-plane angle as a result of the transverse target field. Typically this out-of-plane angle is corrected for in the analysis by calculating the deflection and subtracting it on an event-by-event basis, and the impact on the overall scattering angle, shown in figure 18 is suppressed by power 4. These results are very consistent with the level of change we expect to see for this sort of experiment. Accordingly, we can see that the kinematic coverage of the experiment, and consequently, the targeted physics, is not strongly affected by the target field and chicane, as is shown in Figure 19.

We then consider the main subject of PAC-52’s simulation requirement, namely the detector resolution. The resolution is calculated for each kinematic quantity by subtracting the initial Monte-Carlo generated target quantities from the reconstructed versions. The energy resolution is shown in figure 20. There is a clear broadening by around 5 MeV when the target field and chicane are introduced to the simulation. However, the planned bin size for g_2 ranges from around 30 MeV at the pion production threshold, to 80 MeV at high W , so the resolution shown of around 15 MeV is perfectly acceptable and should not hinder in any way our efforts to resolve the features of g_2 such as the Δ -resonance and other resonances. The systematic impact of the energy resolution is analyzed below in tandem with the scattering angle.

The scattering angle resolution is shown in figures 21 for θ and 22 for ϕ . The impact of the target field slightly increases the width of both peaks to around 15%, or around 1.8 mr. This is small compared to the planned resolution in scattering angle and Q^2 : the scattering angle is used to control the desired Q^2 of the setting, and as is shown in Table 3, the smallest angular resolution needed between settings is around 17 mr. The resolution shown here is much smaller, meaning that there should be no issues resolving the desired features of the moments when they are plotted versus Q^2 .

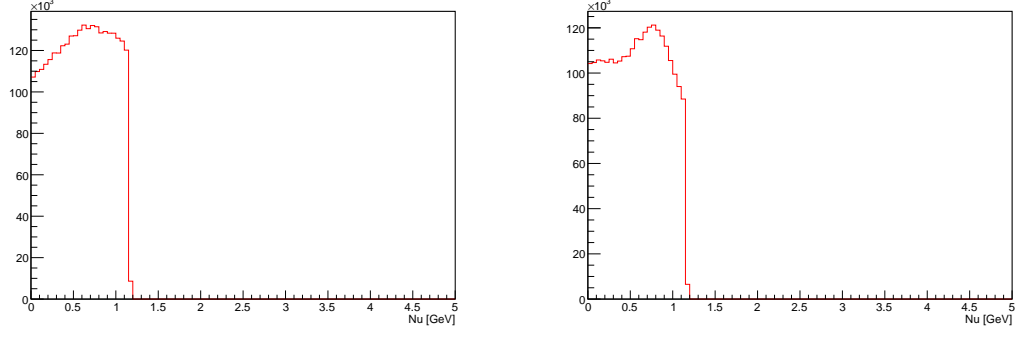


Figure 15: The simulated energy transfer ν for the kinematic setting $p_0=3.607$ GeV, $E_0=4.4$ GeV, $\theta_{\text{Scat}} = 6.5^\circ$. (Left) Without any chicane or target field, (Right) With the transverse target field and chicane accounted for in the simulation.

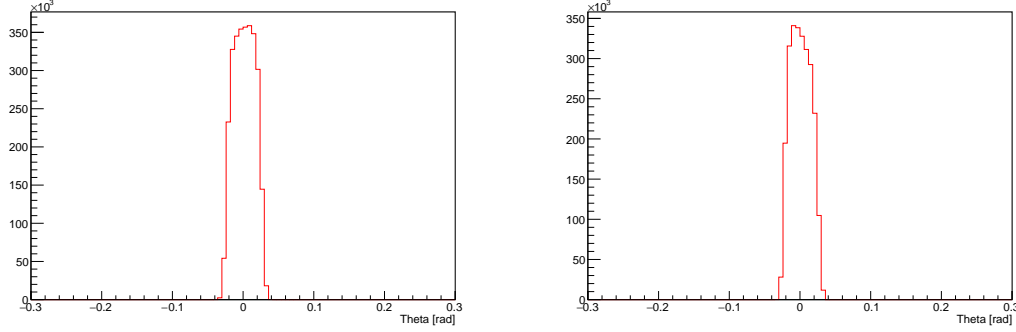


Figure 16: The simulated in-plane scattering angle θ for the kinematic setting $p_0=3.607$ GeV, $E_0=4.4$ GeV, $\theta_{\text{Scat}} = 6.5^\circ$. (Left) Without any chicane or target field, (Right) With the transverse target field and chicane accounted for in the simulation.

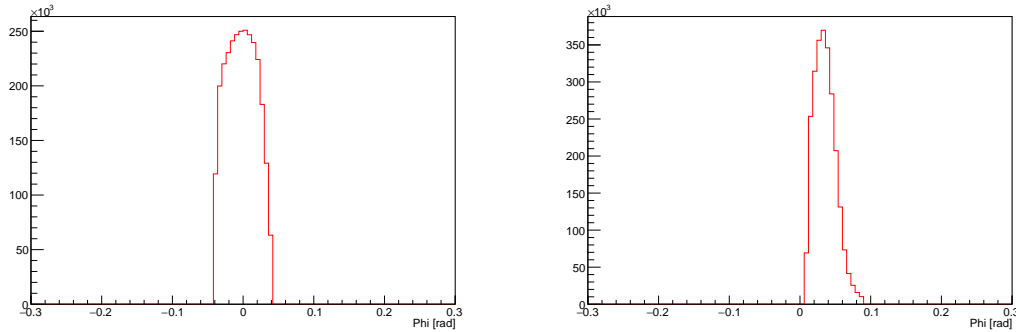


Figure 17: The simulated out-of-plane scattering angle ϕ for the kinematic setting $p_0=3.607$ GeV, $E_0=4.4$ GeV, $\theta_{\text{Scat}} = 6.5^\circ$. (Left) Without any chicane or target field, (Right) With the transverse target field and chicane accounted for in the simulation.

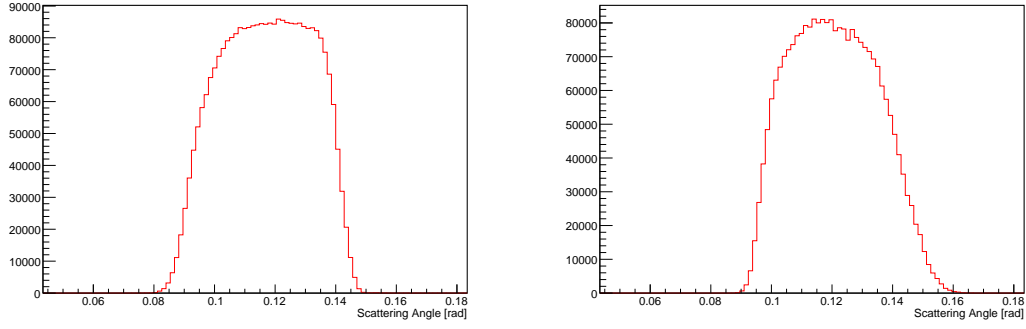


Figure 18: The total scattering angle θ_{Scat} for the kinematic setting $p_0=3.607$ GeV, $E_0=4.4$ GeV, $\theta_{\text{Scat}} = 6.5^\circ$. (Left) Without any chicane or target field, (Right) With the transverse target field and chicane accounted for in the simulation.

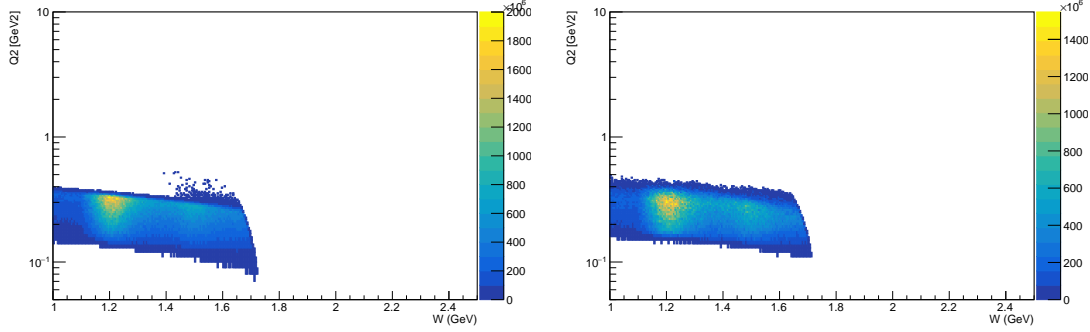


Figure 19: The kinematic coverage in invariant mass W and momentum transfer Q^2 for the kinematic setting $p_0=3.607$ GeV, $E_0=4.4$ GeV, $\theta_{\text{Scat}} = 6.5^\circ$. (Left) Without any chicane or target field, (Right) With the transverse target field and chicane accounted for in the simulation.

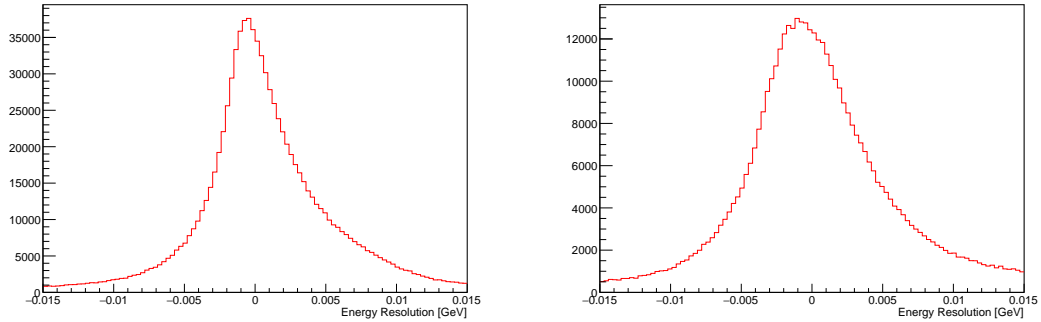


Figure 20: The energy resolution for the kinematic setting $p_0=3.607$ GeV, $E_0=4.4$ GeV, $\theta_{\text{Scat}} = 6.5^\circ$. (Left) Without any chicane or target field, (Right) With the transverse target field and chicane accounted for in the simulation.

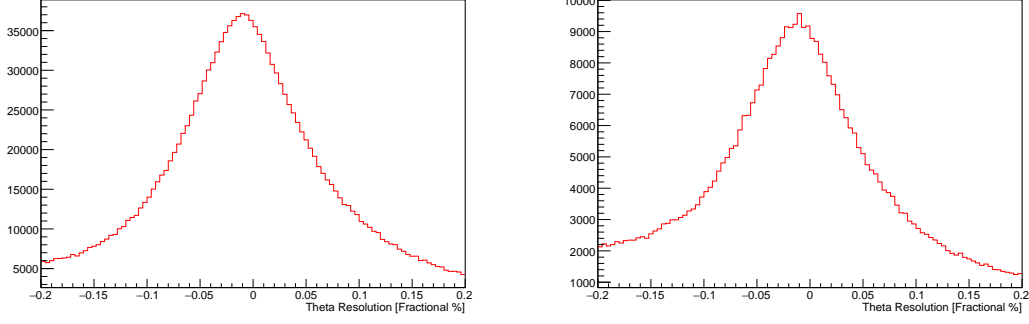


Figure 21: The in-plane scattering angle θ resolution for the kinematic setting $p_0=3.607$ GeV, $E_0=4.4$ GeV, $\theta_{\text{Scat}} = 6.5^\circ$. (Left) Without any chicane or target field, (Right) With the transverse target field and chicane accounted for in the simulation.

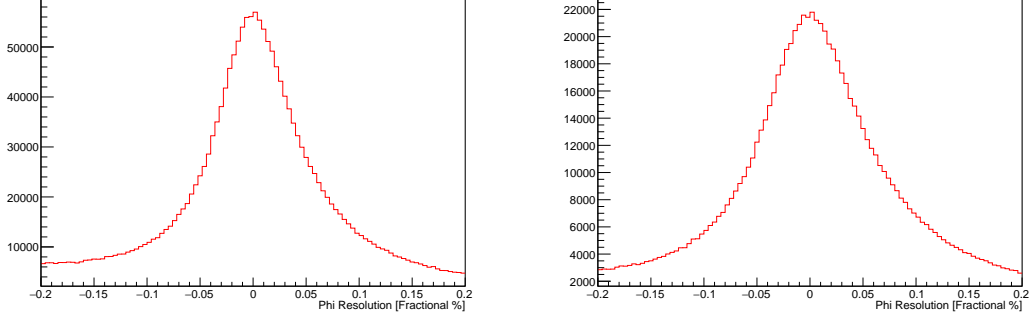


Figure 22: The out-of-plane scattering angle ϕ resolution for the kinematic setting $p_0=3.607$ GeV, $E_0=4.4$ GeV, $\theta_{\text{Scat}} = 6.5^\circ$. (Left) Without any chicane or target field, (Right) With the transverse target field and chicane accounted for in the simulation.

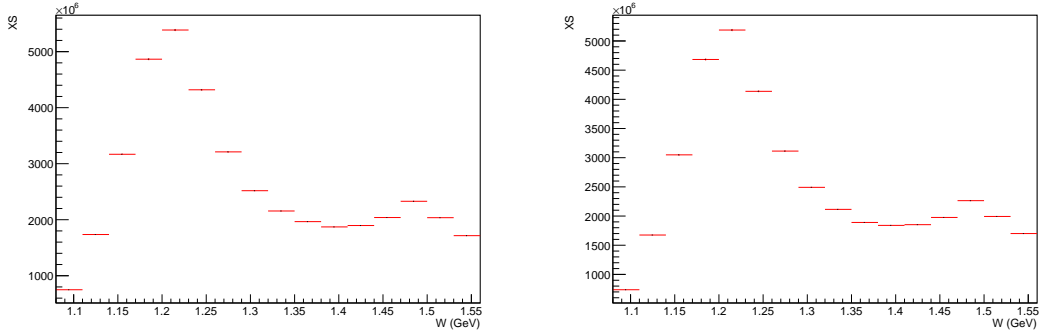


Figure 23: The weighted cross section spectra used to investigate the impact of the reconstruction, for the kinematic setting $p_0=3.607$ GeV, $E_0=4.4$ GeV, $\theta_{\text{Scat}} = 6.5^\circ$. In both cases, the Bosted-Christy model is used to correct the kinematics back to the bin center. Both plots have target field and chicane included in the simulation. (Left) Cross section from generated vertex quantities (Right) Cross section from reconstructed vertex quantities.

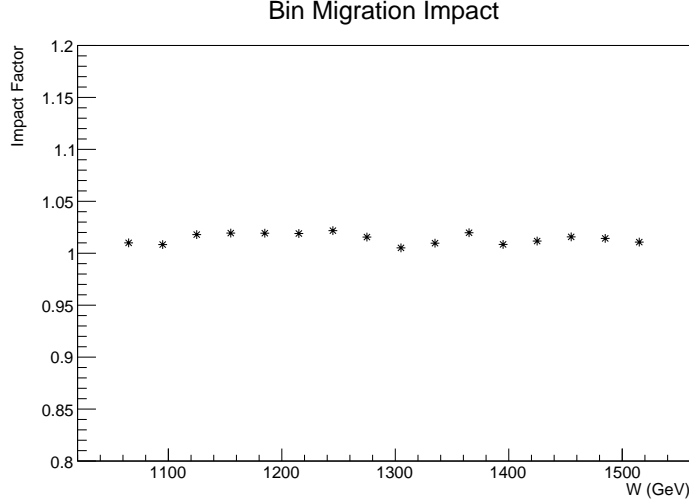


Figure 24: The impact factor for bin-migration **as a result of the resolution** for the kinematic setting $p_0=3.607$ GeV, $E_0=4.4$ GeV, $\theta_{\text{Scat}} = 6.5^\circ$, with target field and chicane included. The impact factor is less than 1.02, or a 2% change at maximum for this setting, and is smaller for all other settings of the experiment.

An enlarged resolution causes some events to migrate to adjacent bins from where they properly should be. This additional bin-migration effect due to the worsened resolution has been studied with the simulation using a realistic cross section model [68]. We bin the simulated events in 30 MeV bins in W and weight by the Bosted cross section model at the bin center, as shown in Figure 23. We compare this cross section before and after the reconstruction to quantify the bin-migration effect of the resolution. Dividing one cross section by the other gives the impact factor of the bin-migration from the resolution. This impact is shown in Figure 24, and is never more than a 2% effect, with a much smaller impact for other kinematic settings. This impact is included in the systematic uncertainties on the cross section of Table 2 and is not a dominating uncertainty. This impact should be evaluated only in terms of the cross section uncertainty as it should not contribute directly to the asymmetry.

Finally, we inspect the overall coverage of the experiment with the target field and chicane included in figure 25. We find that there is no significant shift in the kinematic coverage from the inclusion of the specialized equipment needed, and the resulting coverage is ideal to obtain the desired physics.

In conclusion, performing a full simulation was indeed necessary, and the collaboration now has a comprehensive understanding of the effects of the target field and chicane on the resolution and the physics of the experiment. The impact on the measured quantities and kinematic coverage is small. The impact on the resolution is non-negligible, and quite noticeably smears the resolution peaks as PAC-52 expected, but the change is well within the necessary range to perform the experiment, and correcting for resolution and reconstruction effects will contribute only a trivially small systematic uncertainty.

6 Beamtime Request

The requested beamtime is summarized in Table 4, and is obtained with the rates in Table 3. The count rate of scattered electrons from the polarized target is given by:

$$\dot{N} = \frac{\mathcal{L} \Delta\Omega \Delta E' \sigma}{f} \quad (28)$$

where \mathcal{L} is the luminosity, $\Delta\Omega$ is the angular acceptance, $\Delta E'$ is the momentum bite, σ represents the proton cross section, and f is the dilution factor which accounts for scattering from unpolarized nucleons in the target.

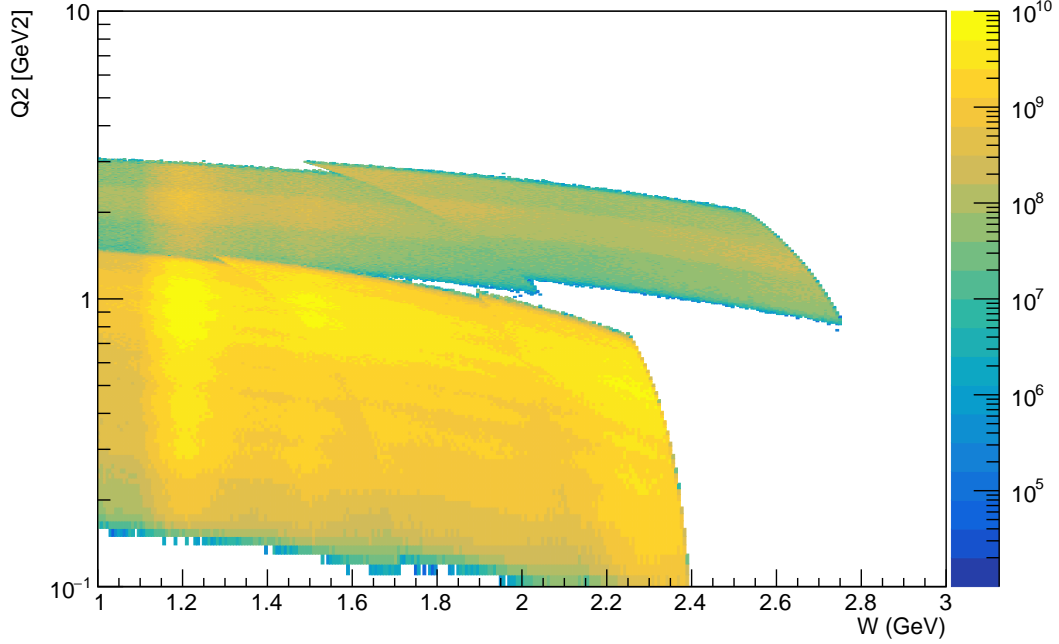


Figure 25: Overall simulated kinematic coverage with transverse target field and chicane magnets included.

We estimate the experimental cross section by combining proton, nitrogen and helium cross sections from the quasifree scattering model QFS [69]. Inelastic and elastic radiative effects are also included. Table 7 shows the assumed material thickness for a 3 cm target.

The time needed for a given uncertainty δA is given by:

$$T = \frac{1}{\dot{N}(fP_bP_T\delta A)^2} \quad (29)$$

The relevant statistical uncertainty is for the asymmetry, even though this is a cross section measurement, because in the product σA the dominant error arises from A .

The calculated rates were shown in Table 3. The sixth column represents the rate (in each bin) from the proton, while the seventh shows the total prescaled rate seen by the spectrometer. We assume that the DAQ limit is at least 40 kHz[51]. Initial calculations of the rates are generally far below this limit, eliminating the need for a prescale factor.

As discussed previously, time requested is chosen to bring the statistical error on the moments to the 5-8% range. In general, given the high rate at lower Q^2 , this precision can be obtained quickly for many of the settings, but will require more PAC days for the highest kinematics requested.

The choice of parameters used in our rate calculation is summarized in Table 7. We assume an angular acceptance of 5.4 msr and a momentum acceptance of $-10\% < dp < +22\%$, and beam and target polarizations of 80 and 75% respectively. We note that higher polarization values are routinely achieved. Finally, we assume that the minimum time that we would reasonably spend at each setting is one half hour, regardless of how high the rate is.

6.1 Overhead

The incident beam causes radiation damage in the frozen ammonia, which leads to the creation of atomic hydrogen in the target material. This provides an additional relaxation path for the nuclear spins, and the buildup of these free radicals leads to a gradual decay of the target polarization. The concentration of these unwanted radicals can be reduced significantly by raising the temperature of the target to 80-90K, in a process known as annealing. Given the proposed beam current and raster size,

we expect to require an anneal about once every 14 hours of beam time. The anneal itself typically requires 2.5 hours from start to beam back on target. The target stick holds two ammonia batches. Each batch can absorb approximately $17 \cdot 10^{15}$ e-/cm², at which point the material must be replaced. We expect to swap out target inserts about once every 5 days of accumulated (100% efficient) beam, so we should require three target sticks, for a total of two swaps. To replace the stick and calibrate the NMR instrumentation requires about half a shift.

One final overhead arising from the target comes from the need for dedicated empty cell and carbon target runs, which are used to determine the granular target packing fraction and dilution factor. These high rate unpolarized runs can be completed in about one half hour, and we plan to perform them for every other momentum setting.

The experiment should only require one pass change, estimated to require 4 hours. Changing the spectrometer momentum settings requires approximately 15 minutes each on average. We will perform one Møller measurement for each beam energy, each of which requires two hours.

The higher Q^2 points may have a significant positron background from pair production which will need to be accounted for, requiring around an hour of data as well as a ramp down and up of the dipole to change the polarity. The changing of the dipole field can be performed in parallel with other overhead tasks such as TEs, but we estimate the overall time at 4 hours per measurement.

The overhead requirement is summarized in Table 5. We note that previous experience has shown that many overhead tasks can be performed in parallel, or scheduled to coincide with non-delivery of beam. In this sense, our overhead estimate should be conservative.

Beam Energy (GeV)	Beam Current (nA)	Beam Requirements	Target Material	Material Thickness (mg/cm ²)	Beamtime (days)
4.4	85	Polarized	NH ₃	261.6	11.2
8.8	85	Polarized	NH ₃	261.6	1.8
Total Time					13.0

Table 4: Production data beam requirements and time request

Table 5: Overhead

Overhead	Number	Time Per (hr)	(hr)
Target anneal	26	2	52
Beamline survey	10	8	80
Target swap	2	4	8
Target T.E.	6	2.25	13.5
Target field ramp	10	1	10
Carbon, Empty, & Dummy Runs	28	0.50	14
Pass change	2	4	8
Momentum change	28	0.50	14.0
Moller measurement	10(+1 shift)	4	48
Pair-symmetric background measurement	2	4	8
Optics/elastic calibration	2	16	32
BCM calibration	2	4	8
295.5 (13 Days)			

Table 6: Statistical Uncertainty

Kinematic	A error	A _⊥ error
1	0.012	0.010
2	0.013	0.011
3	0.014	0.012
4	0.015	0.012
5	0.016	0.013

Parameter	Value
$\Delta\Omega$ [msr]	5.4
$\pm\delta P$ [%]	16.0
T_b	0.032
T_a	0.032
Minimum time per setting [hr]	1.0
Minimum Momentum [MeV]	500.0
Maximum Momentum [MeV]	9000.0
Daq Limit [kHz]	40.0
Packing Fraction	0.55

Table 7: Experiment Parameters

6	0.017	0.012
7	0.017	0.013
8	0.016	0.012
9	0.016	0.021
10	0.016	0.032

* EG4 expected uncertainty.

7 Summary

We request 26 days in order to perform a precision measurement of g_2^p in the transition region using a transversely polarized proton (NH_3) target, together with the SHMS detector. This measurement will require the use of a Slow Raster and Chicane magnets, and relies on techniques which have been tested and proven successful by a number of other experiments.

The experiment will measure polarized transverse asymmetries and unpolarized cross sections for the proton from an ammonia (NH_3) target. These will be used together to form perpendicular polarized cross section differences. These will be combined with world data at the same kinematics for the parallel polarized cross section to construct the structure function g_2 .

This measurement will address a sizeable gap in the measured coverage of g_2 for the proton, and with it, produce several valuable moments which can assist in testing theoretical predictions such as current and future predictions of Lattice QCD. We will also employ the new data on fundamental observable g_2 to contribute to advances in our understanding of higher twist effects by comparison to g_2^{WW} , and connect our results to the TMD distribution functions through the calculation of g_T .

The data will probe the nucleon polarizabilities, with a focus on the wide variation in JLab \bar{d}_2 results, and further investigate the interesting result produced by the SANE experiment by filling in the missing region in Q^2 where the sign of \bar{d}_2 is expected to flip. The results will also provide data useful for constructing the hyperfine integral Δ_2 , which requires measurements of g_2 across a broad spectrum of Q^2 up to around 1.1 GeV^2 .

Finally, we have performed a full simulation in accordance with PAC-52's requirement for the removal of the conditional status. This has proven to be a necessary and valuable check as the simulation has provided us with greatly enhanced understanding of the resolution and the impact of the target field. The results demonstrate the experiment to be very feasible and the impact of the target field and chicane to now be well understood.

This proposal aims to take advantage of an opportunity to measure an important quantity in a region which can be much more easily accessed experimentally than many of its predecessors. This region is ripe with opportunity for further understanding the transition region of QCD, and comparison with upcoming proposals of Lattice QCD. For a comparatively small experimental cost, we will obtain a high precision test of a number of different facets of QCD, and enhance our understanding of the crucial transition between perturbative QCD and low Q^2 effective theories.

References

- [1] 2023 low-q workshop. Chania, Greece.
- [2] C. G. Callan and David J. Gross. High-energy electroproduction and the constitution of the electric current. *Phys. Rev. Lett.*, 22:156–159, Jan 1969.
- [3] R. L. Jaffe. $G(2)$: The Nucleon’s Other Spin Dependent Structure Function. *Comments Nucl. Part. Phys.*, 19:239, 1990.
- [4] Alberto Accardi and Alessandro Bacchetta. Accessing the nucleon transverse structure in inclusive deep inelastic scattering. *Physics Letters B*, 773:632–638, 2017.
- [5] Alberto Accardi, Alessandro Bacchetta, W. Melnitchouk, and Marc Schlegel. What can break the wandzura-wilczek relation? *Journal of High Energy Physics*, 2009(11):093, nov 2009.
- [6] S. Wandzura and Frank Wilczek. Sum rules for spin dependent electroproduction: Test of relativistic constituent quarks. *Phys. Lett.*, B72:195, 1977.
- [7] D. Drechsel, S. S. Kamalov, and L. Tiator. Unitary Isobar Model – MAID2007. *The European Physical Journal A*, 34(1):69, 2007.
- [8] F. R. Wesselmann, K. Slifer, S. Tajima, et al. Proton Spin Structure in the Resonance Region. *Phys. Rev. Lett.*, 98:132003, 2007.
- [9] W. Armstrong et al. Revealing color forces with transverse polarized electron scattering. *Phys. Rev. Lett.*, 122:022002, Jan 2019.
- [10] Robert Fersch et al. Determination of the Proton Spin Structure Functions for $0.05 < Q^2 < 5 \text{ GeV}^2$ using CLAS. *Phys. Rev. C*, 96:065208, Dec 2017.
- [11] X. Zheng, A. Deur, H. Kang, et al. Measurement of the proton spin structure at long distances. *Nature Physics*, 17:736–741, 2021.
- [12] R. L. Jaffe and Xiang-Dong Ji. Studies of the Transverse Spin Dependent Structure Function $g(2)$ (X, Q^2). *Phys. Rev. D*, 43:724–732, 1991.
- [13] V. M. Braun, T. Lautenschlager, A. N. Manashov, and B. Pirnay. Higher twist parton distributions from light-cone wave functions. *Phys. Rev. D*, 83:094023, May 2011.
- [14] Yuri V. Kovchegov, Daniel Pitonyak, and Matthew D. Sievert. Helicity evolution at small x : Flavor singlet and nonsinglet observables. *Phys. Rev. D*, 95:014033, Jan 2017.
- [15] S. Kumano and Qin-Tao Song. Transverse-momentum-dependent parton distribution functions up to twist 4 for spin-1 hadrons. *Phys. Rev. D*, 103:014025, Jan 2021.
- [16] S. D. Drell and A. C. Hearn. Exact Sum Rule for Nucleon Magnetic Moments. *Phys. Rev. Lett.*, 16:908–911, 1966.
- [17] D. Drechsel, S. S. Kamalov, and L. Tiator. Gerasimov-Drell-Hearn Sum Rule and Related Integrals. *Phys. Rev. D*, 63:114010, 2001.
- [18] Xiang-Dong Ji and Jonathan Osborne. Generalized sum rules for spin-dependent structure functions of the nucleon. *J. Phys.*, G27:127, 2001.
- [19] D. Drechsel, B. Pasquini, and M. Vanderhaeghen. Dispersion Relations in Real and Virtual Compton Scattering. *Phys. Rept.*, 378:99–205, 2003.
- [20] Z. E. Meziani et al. Higher twists and color polarizabilities in the neutron. *Phys. Lett.*, B613:148–153, 2005.
- [21] O. A. Rondon. The RSS and SANE Experiments at Jefferson Lab. *AIP Conference Proceedings*, 1155(1):82–92, 2009.

- [22] D. Flay et al. Measurements of d_2^n and A_1^n : Probing the neutron spin structure. *Phys. Rev. D*, 94:052003, Sep 2016.
- [23] M. Gockeler, R. Horsley, W. Kurzinger, H. Oelrich, D. Pleiter, Paul E. L. Rakow, A. Schafer, and G. Schierholz. A Lattice calculation of the nucleon’s spin dependent structure function $g(2)$ revisited. *Phys. Rev. D*, 63:074506, 2001.
- [24] P. L. Anthony et al. Precision measurement of the proton and deuteron spin structure functions g_2 and asymmetries $a(2)$. *Phys. Lett.*, B553:18–24, 2003.
- [25] P.L. Anthony et al. Precision Measurement of the Proton and Deuteron Spin Structure Functions g_2 and Asymmetries A_2 . *Physics Letters B*, 553(1-2):18 – 24, 2003.
- [26] F. R. Wesselmann et al. Proton Spin Structure in the Resonance Region. *Phys. Rev. Lett.*, 98:132003, 2007.
- [27] K. Slifer et al. ^3He Spin-Dependent Cross Sections and Sum Rules. *Phys. Rev. Lett.*, 101:022303, 2008.
- [28] I.I. Balitsky, V.M. Braun, and A.V. Kolesnichenko. Power corrections $1/q^2$ to parton sum rules for deep inelastic scattering from polarized nucleons. *Physics Letters B*, 242(2):245–250, 1990.
- [29] A.I. Signal. Calculations of higher twist distribution functions in the MIT bag model. *Nuclear Physics B*, 497(1-2):415–434, jul 1997.
- [30] X. Song, *Phys. Rev. D* **54**, 1955 (1996).
- [31] H. Weigel and L. Gamberg, *Nucl. Phys. A* **680**, 48 (2000);.
- [32] M. Osipenko et al. Global analysis of data on the proton structure function g_1 and extraction of its moments. *Phys. Rev.*, D71:054007, 2005.
- [33] Jose Manuel Alarcón, Franziska Hagelstein, Vadim Lensky, and Vladimir Pascalutsa. Forward doubly-virtual compton scattering off the nucleon in chiral perturbation theory. ii. spin polarizabilities and moments of polarized structure functions. *Phys. Rev. D*, 102:114026, Dec 2020.
- [34] Y. Prok, P. Bosted, V.D. Burkert, A. Deur, K.V. Dharmawardane, G.E. Dodge, K.A. Griffioen, S.E. Kuhn, R. Minehart, et al. Moments of the spin structure functions and for g_1^p and g_1^d for $0.05 < Q^2 < 3.0 \text{ GeV}^2$. *Physics Letters B*, 672(1):12 – 16, 2009.
- [35] Aldo Antognini, Franziska Hagelstein, and Vladimir Pascalutsa. The Proton Structure in and out of Muonic Hydrogen. *Annual Review of Nuclear and Particle Science*, 72:389–418, September 2022.
- [36] C. E. Carlson, V. Nazaryan, and K. Griffioen. Proton Structure Corrections to Electronic and Muonic Hydrogen Hyperfine Splitting. *Phys. Rev. A*, 78:022517, 2008.
- [37] David Ruth, Karl Slifer, Jian-Ping Chen, Carl E. Carlson, Franziska Hagelstein, Vladimir Pascalutsa, Alexandre Deur, Sebastian Kuhn, Marco Ripani, Xiaochao Zheng, Ryan Zielinski, and Chao Gu. New spin structure constraints on hyperfine splitting and proton zemach radius. *Physics Letters B*, 859:139116, 2024.
- [38] M. Battaglieri, R. De Vita, A. Deur, M. Ripani, et al. Jefferson Lab CLAS EG4 Run Group. <http://www.jlab.org/expprog/proposals/03/PR03-006.pdf>.
- [39] D. Ruth, R. Zielinski, C. Gu, et al. Proton spin structure and generalized polarizabilities in the strong quantum chromodynamics regime. *Nature Physics*, 2022.
- [40] J. Benesch. Proof of principle design for pre-chicane for use with 5T transverse solenoid for high current in Hall C, small SHMS angles in Hall C, or SoLID. Technical report, 2024.
- [41] K. Slifer et al. The Deuteron Tensor Structure Function b_1 . Jefferson Lab E12-13-011.

- [42] E. Long et al. Measurements of the Quasi-Elastic and Elastic Deuteron Tensor Asymmetries. Jefferson Lab E12-15-005.
- [43] J. Benesch. Examination of the need for an upstream chicane for proposal "A Measurement of the Proton g_2 Structure Function at Intermediate Q^2 ". Technical report, 2023.
- [44] J. Benesch. Private conversation.
- [45] D. Gaskell. Private conversation.
- [46] Hall C Standard Equipment Manual 2019. <https://hallcweb.jlab.org/safety-docs/current/Standard-Equipment-Manual.pdf>.
- [47] D. Mack. Private conversation.
- [48] J. Alcorn et al. Basic Instrumentation for Hall A at Jefferson Lab. *Nucl. Instrum. Meth.*, A522:294–346, 2004.
- [49] W. Barletta. Unit 11 - Lecture 18 Synchrotron Radiation - I, MIT Summer School. https://uspas.fnal.gov/materials/09UNM/Unit_11_Lecture_18_Synchrotron_radiation.pdf.
- [50] C. Harris. *The Proton Coulomb Form Factor from Polarized Inclusive e - p Scattering*. PhD thesis, University of Virginia, 2001.
- [51] D. Camsonne. Private conversation.
- [52] J. Beringer et al. Review of Particle Physics. *Phys. Rev. D*, 86:010001, 2012.
- [53] J. Singh and V. Sulkosky. Radiation Thickness, Collisional Thickness, and Most Probable Collisional Energy Loss for E97-110. Technical report, E97-110 Collaboration, 2007. http://hallaweb.jlab.org/experiment/E97-110/tech/radlength_sagdhv130.pdf.
- [54] R. L. Jaffe and X.-D. Ji. Studies of the Transverse Spin-Dependent Structure Function $g_2(x, Q^2)$. *Phys. Rev. D*, 43:724–732, 1991.
- [55] Aneesh V. Manohar. An introduction to spin dependent deep inelastic scattering, 1992.
- [56] M. Amarian et al. Measurement of the Generalized Forward Spin Polarizabilities of the Neutron. *Phys. Rev. Lett.*, 93:152301, 2004.
- [57] F. Garibaldi spokespersons. J. P. Chen, A. Deur. Jlab experiment e97-110.
- [58] K. Slifer, E94010 Technical Note #37 : "Dependence of the Cross-Section on Acceptance Cuts for E94010", (2001).
- [59] K. Slifer, E94010 Technical Note #38 : "E94010 Unpolarized ^3He Cross Sections", (2001).
- [60] K. Slifer, Ph.D. Thesis. Temple University (2004).
- [61] Earle L. Lomon. Effect of recent $R(p)$ and $R(n)$ measurements on extended Gari-Kruempelmann model fits to nucleon electromagnetic form factors. *Phys. Rev.*, C66:045501, 2002.
- [62] A. W. Thomas and W. Weise. *The Structure of the Nucleon*. Wiley, Berlin, 2001.
- [63] D. Ruth. *A Strong-QCD Regime Measurement of the Proton's Spin Structure*. PhD thesis, University of New Hampshire, 2022.
- [64] Y. B. Dong. Twist-3 effects and target mass corrections. *Phys. Rev.*, C77:015201, 2008.
- [65] D. Gaskell. Overview and Use of SIMC. 2022.
- [66] Kyoko Makino. COSY Infinity.
- [67] R. Bodenstein. Next-Step Optimization for Hall C Pre-Chicane For Use With 5 T Transverse Solenoid - JLAB-TN-25-023 . Technical report, 2025.

- [68] M. E. Christy and P. E. Bosted. Empirical fit to precision inclusive electron–proton cross sections in the resonance region. *Phys. Rev. C*, 81:055213, 2010.
- [69] J.S. O’Connell and Lightbody J.W. Jr. Modeling Single Arm Electron Scattering and Nucleon Production From Nuclei by GeV Electrons. *Comput. Phys.; (United States)*, 2:3, 1988.

Supplemental Materials

Dr. Ryan Bodenstein - Bmad Chicane Simulation Technote

For the PAC’s ease of access, we include on the following pages the tech note by Dr. Ryan Bodenstein referenced earlier in the text discussing his optimization of Dr. Benesch’s chicane design with Bmad.

Dr. Jay Benesch - Preliminary Chicane Technote

For the PAC’s ease of access, we include on the following pages the tech note by Dr. Jay Benesch referenced earlier in the text discussing his new chicane design.

Next-Step Optimization for Hall C Pre-Chicane For Use With 5 T Transverse Solenoid JLAB-TN-25-023

Ryan Bodenstein, ryanmb@jlab.org

Original: April 14, 2025
This Revision (1): April 14, 2025

1 Document Description

This document details the next-level study for the work first presented in JLAB-TN-24-007 (by Jay Benesch), where the proof-of-principle was first performed. The work presented in this Tech Note takes the section of beamline described in TN-24-007, and optimizes specific parameters. This work involved translating the lattice from OptiM to MAD8/X to Bmad (thanks to Kirsten Deitrick for running the translation script!). The optimization was performed in Bmad.

This note will briefly summarize the work, and present the results.

2 Method

1. Convert OptiM files to MAD8 or MADX (MAD for the rest of the document). Do this for all three passes given (Passes 2, 4, and 5).
2. Convert from MAD to Bmad using the python scripts provided by Bmad.
3. Check each line in Bmad to be sure it converted properly to first order.
4. Combine all lines into the same simulation, so that all three passes can be seen and optimized simultaneously.
5. Determine constraints and goals.
6. Determine variables.
7. Write overlays for drifts, and set limits on variables.
8. Run optimizers to reach constraints and goals.

3 Constraints and Goals

- The solenoid (modeled as two dipoles) cannot change in strength. The target is in the center of the two dipoles.
- The target inside the solenoid is 2 cm above the entering beamline.
- The dump target is also 2 cm above the entering beamline.
- The center of the central dipole must align in Z-coordinates for all passes, so that the dipole can be adjusted by simply changing its Y-position.
- The target in the solenoid must align in the Z-coordinates for all passes.

Please note, the simulations performed here did not translate the entrance of the beamline to machine coordinates, so all measurement are relative to this.

4 Variables

- Dipole 1 and Dipole 2 can change in strength for each pass.
- The drifts in between Dipole 1 and Dipole 2, as well as those between Dipole 2 and the Solenoid, can be adjusted, so long as the total length remains the same, or the target in the solenoid is in the correct Z-coordinates for all passes.

5 Results

Here, the results of the simulations are presented.

5.1 Floor Plans

In the following floor plans, pay close attention to the axis labels. First, the coordinates of primary concern are the Y-Z plane. Then, for completeness, the X-Z plane will be shown, as well as the β functions in the region. This beamline contains no quadrupoles, so all elements are either dipoles (blue), monitors/-correctors/etc... (orange), or the orbit (green).

First, the Y-Z Plane (Figures 1, 2, 3) is shown.

Next, the X-Z Plane (Figures 4, 5) is shown.

Finally, a glance at the β functions (Figure 6) is shown.

5.2 Data

In the tables below, the floor coordinates are shown for each pass. Universe 1 is Pass 2 (Table 1), Universe 2 is Pass 4 (Table 2), and Universe 3 is Pass 5 (Table 3).

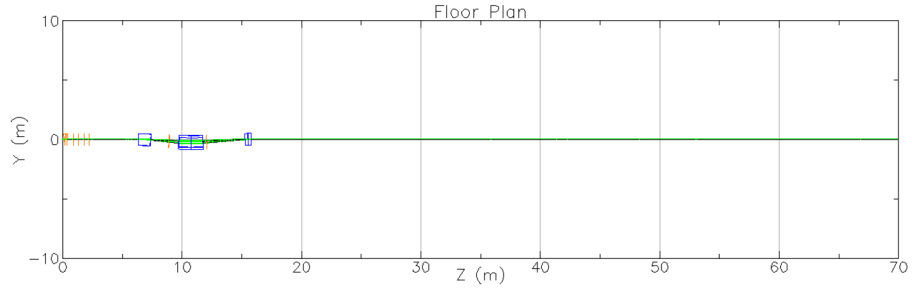


Figure 1: Floor plan in the Y-Z plane showing the full length of the beamline in question. Green is the orbit going through the line. Blue are dipoles, and orange represent other elements.

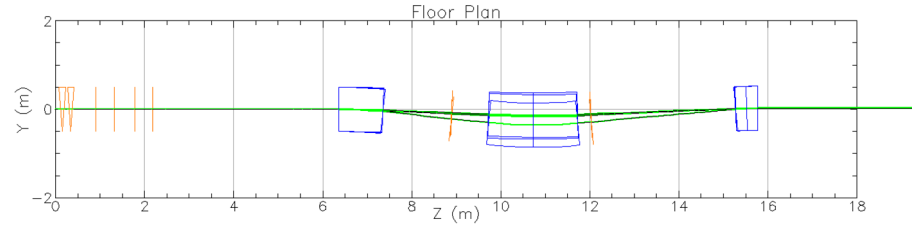


Figure 2: Floor plan in the Y-Z plane, zooming in on the region of the chicane. Green is the orbit going through the line. Blue are dipoles, and orange represent other elements.

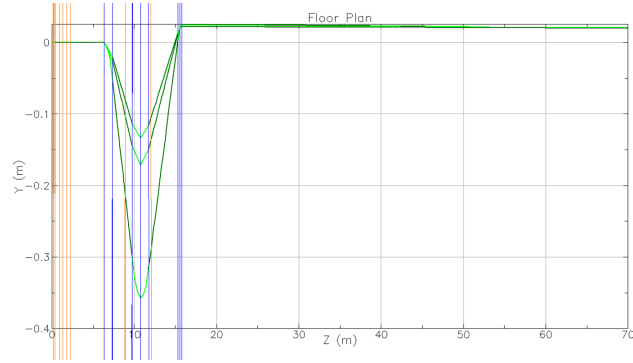


Figure 3: Floor plan in the Y-Z plane, with the axes adjusted so that the small details can be shown. Green is the orbit going through the line. Blue are dipoles, and orange represent other elements.

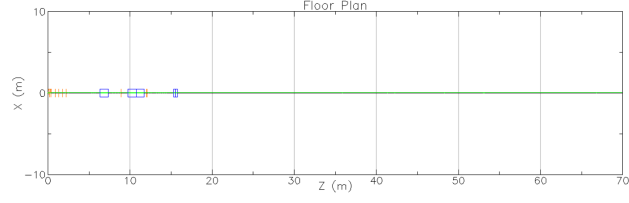


Figure 4: Floor plan in the X-Z plane showing the full length of the beamline in question. Green is the orbit going through the line. Blue are dipoles, and orange represent other elements.

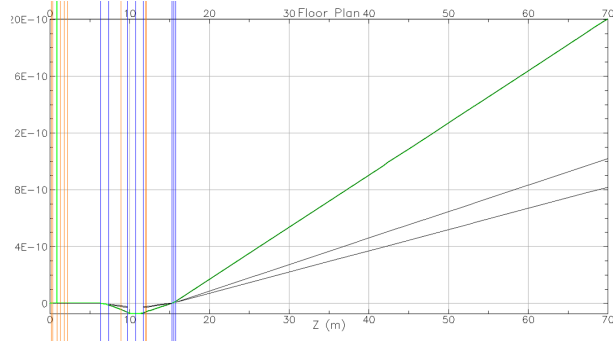


Figure 5: Floor plan in the X-Z plane, with the axes adjusted so that the small details can be shown. Green is the orbit going through the line. Blue are dipoles, and orange represent other elements. Vertical axis is X (m). Vertical span is 0-1 nm.

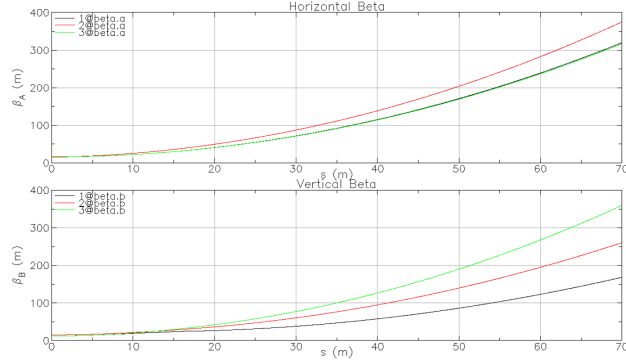


Figure 6: β for each plane.

5.3 Magnet and Drift Settings After Optimization

After optimizations, the settings for Dipole 1 and Dipole 2 were altered for each pass. Please note, Dipole 2 is split in halves, and each half has the same

strength. The new values (to the precision of the simulation - not all are significant figures) are below:

Dipole 1, Pass 2: 1.5632267536884163E+00 T
Dipole 1, Pass 4: 1.4888515664951818E+00 T
Dipole 1, Pass 5: 1.4513247769702611E+00 T
Half of Dipole 2, Pass 2: -1.4518423115716796E+00 T
Half of Dipole 2, Pass 4: -1.4146546227064962E+00 T
Half of Dipole 2, Pass 5: -1.3958912166044295E+00 T

Similarly, in order to align the center of the second dipole and the target inside the solenoid, two drifts were altered. This is a "quick and dirty" method of aligning the elements for each pass, rather than the more detailed method, which would require writing proper patches, calculating exit angles, entrance angles, and writing the appropriate coordinate changes (via patches) to make sure all of the magnets align on the floor as they would in the real machine. For the purposes of this study, the simple adjustments should suffice. Each pass will have a different length, as the path length through the dipoles differs for the different energies (beam rigidity). This adjustment allows for a quick alignment.

One of the drifts before Dipole 2 is now of length (drift name in parenthesis after value):

Pass 2: 8.4323583381409484E-01 m (OD15)
Pass 4: 8.3033186862547459E-01 m (OD151)
Pass 5: 8.2881578468939832E-01 m (OD151)

Another drift, located between Dipole 2 and the Solenoid, was adjusted in a similar manner:

Pass 2: 3.1767364025027950E-01 m (OD16)
Pass 4: 3.0568467549769601E-01 m (OD152)
Pass 5: 3.0420944640403369E-01 m (OD152)

6 Conclusions

This document shows that it is possible to use the chicane in a manner described in the original proof-of-principle work in Jay's TN-24-007. That work was very close to the proper numbers, and this work shows that the exact values are achievable.

If this proposal proceeds, a more strict simulation can be performed to be sure all optics are correct, as well as any "quick-and-dirty" approximations addressed.

Table 1: Pass 2 Floor Coordinates (Universe 1)

Index Units	Name	Type	s m	l m	X m	Y m	Z m
0	BEGINNING	Beginning-Ele	0	—	0	0	0
1	IIPM3H02	Monitor	0	0	0	0	0
2	OD0	Drift	0.07214	0.07214	0	0	0.07214
3	KMBD3H02V	Kicker	0.22214	0.15	0	0	0.22214
4	OD1	Drift	0.26733	0.04519	0	0	0.26733
5	KMBD3H02H	Kicker	0.41733	0.15	0	0	0.41733
6	OD2	Drift	0.90622	0.48889	0	0	0.90622
7	KMFR3H03H	Kicker	0.90622	0	0	0	0.90622
8	OD3	Drift	1.31245	0.40623	0	0	1.31245
9	KMFR3H03V	Kicker	1.31245	0	0	0	1.31245
10	OD4	Drift	1.77586	0.46341	0	0	1.77586
11	KMFR3H04H	Kicker	1.77586	0	0	0	1.77586
12	OD5	Drift	2.18209	0.40623	0	0	2.18209
13	KMFR3H04V	Kicker	2.18209	0	0	0	2.18209
14	OD6	Drift	2.4805	0.29841	0	0	2.4805
15	IIPM3H04	Monitor	2.4805	0	0	0	2.4805
16	OD7	Drift	5.3625	2.882	0	0	5.3625
17	IIBC3H04A	Monitor	5.3625	0	0	0	5.3625
18	OD8	Drift	5.5625	0.2	0	0	5.5625
19	IIBC3H04B	Monitor	5.5625	0	0	0	5.5625
20	OD9	Drift	5.7625	0.2	0	0	5.7625
21	IIBC3H04C	Monitor	5.7625	0	0	0	5.7625
22	OD10	Drift	6.35579	0.59329	0	0	6.35579
23	BDIP1	SBend	7.35579	1	0	-0.05222	7.35397
24	OD11	Drift	7.95816	0.60237	0	-0.11506	7.95305
25	IIBC3H05	Monitor	7.95816	0	0	-0.11506	7.95305
26	OD12	Drift	8.26816	0.31	0	-0.14741	8.26136
27	IUN3H05	Monitor	8.26816	0	0	-0.14741	8.26136
28	OD13	Drift	8.57816	0.31	0	-0.17975	8.56967
29	IIBC3H05A	Monitor	8.57816	0	0	-0.17975	8.56967
30	OD14	Drift	8.89756	0.3194	0	-0.21308	8.88733
31	KMBD3H05V	Kicker	8.89756	0	0	-0.21308	8.88733
32	OD15	Drift	9.7408	0.84324	0	-0.30106	9.72596
33	BDIP2	SBend	10.7408	1	0	-0.35699	10.724
34	IMIDPT	Monitor	10.7408	0	0	-0.35699	10.724
35	BDIP2	SBend	11.7408	1	0	-0.31593	11.72276
36	OD16	Drift	12.05847	0.31767	0	-0.28749	12.03916
37	KMAP3H07H	Kicker	12.05847	0	0	-0.28749	12.03916
38	OD17	Drift	12.35297	0.2945	0	-0.26113	12.33248
39	IIPM3H07A	Monitor	12.35297	0	0	-0.26113	12.33248
40	OD18	Drift	12.60595	0.25298	0	-0.23849	12.58444
41	IHA3H07A	Monitor	12.60595	0	0	-0.23849	12.58444
42	OD19	Drift	13.30655	0.7006	0	-0.17578	13.28223
43	IIPM3H07B	Monitor	13.30655	0	0	-0.17578	13.28223
44	OD20	Drift	13.56885	0.2623	0	-0.1523	13.54348
45	IIBC3H07	Monitor	13.56885	0	0	-0.1523	13.54348
46	OD21	Drift	13.79624	0.22739	0	-0.13195	13.76996
47	IYG3H07	Monitor	13.79624	0	0	-0.13195	13.76996
48	OD22	Drift	14.01011	0.21387	0	-0.1128	13.98297
49	IHA3H07B	Monitor	14.01011	0	0	-0.1128	13.98297
50	OD23	Drift	14.26909	0.25898	0	-0.08962	14.24091
51	IIPM3H07C	Monitor	14.26909	0	0	-0.08962	14.24091
52	OD24	Drift	14.49309	0.224	0	-0.06957	14.46401
53	IVBV3H07	Monitor	14.49309	0	0	-0.06957	14.46401
54	OD25	Drift	15.30623	0.81314	0	0.00321	15.27389
55	BSOL1	SBend	15.55623	0.25	0	0.02	15.5233
56	IPIVOTC	Monitor	15.55623	0	0	0.02	15.5233
57	BSOL1	SBend	15.80623	0.25	0	0.02558	15.77322
58	OD26	Drift	35.92923	20.123	0	0.02351	35.89622
59	IIPM3H08	Monitor	35.92923	0	0	0.02351	35.89622
60	OD27	Drift	41.43223	5.503	0	0.02294	41.39922
61	IIPM3H09	Monitor	41.43223	0	0	0.02294	41.39922
62	OD28	Drift	42.37053	0.9383	0	0.02284	42.33752
63	IITV3H10	Monitor	42.37053	0	0	0.02284	42.33752
64	OD29	Drift	48.37623	6.0057	0	0.02222	48.34322
65	IIDP3H10	Monitor	48.37623	0	0	0.02222	48.34322
66	OD30	Drift	53.07623	4.7	0	0.02174	53.04322
67	IITV3H10A	Monitor	53.07623	0	0	0.02174	53.04322
68	OD31	Drift	53.24623	0.17	0	0.02172	53.21322
69	IIDW3H10	Monitor	53.24623	0	0	0.02172	53.21322
70	OD32	Drift	66.93623	13.69	0	0.02031	66.90322
71	DIIBD3H10	Drift	69.93623	3	0	0.02	69.90322
72	IIBD3H10	Monitor	69.93623	0	0	0.02	69.90322
73	END	Marker	69.93623	0	0	0.02	69.90322

Table 2: Pass 4 Floor Coordinates (Universe 2)

Index Units	Name	Type	s m	l m	X m	Y m	Z m
0	BEGINNING	Beginning-Ele	0	—	0	0	0
1	IIPM3H02	Monitor	0	0	0	0	0
2	OD136	Drift	0.07214	0.07214	0	0	0.07214
3	KMBD3H02V	Kicker	0.22214	0.15	0	0	0.22214
4	OD137	Drift	0.26733	0.04519	0	0	0.26733
5	KMBD3H02H	Kicker	0.41733	0.15	0	0	0.41733
6	OD138	Drift	0.90622	0.48889	0	0	0.90622
7	KMFR3H03H	Kicker	0.90622	0	0	0	0.90622
8	OD139	Drift	1.31245	0.40623	0	0	1.31245
9	KMFR3H03V	Kicker	1.31245	0	0	0	1.31245
10	OD140	Drift	1.77586	0.46341	0	0	1.77586
11	KMFR3H04H	Kicker	1.77586	0	0	0	1.77586
12	OD141	Drift	2.18209	0.40623	0	0	2.18209
13	KMFR3H04V	Kicker	2.18209	0	0	0	2.18209
14	OD142	Drift	2.4805	0.29841	0	0	2.4805
15	IIPM3H04	Monitor	2.4805	0	0	0	2.4805
16	OD143	Drift	5.3625	2.882	0	0	5.3625
17	IIBC3H04A	Monitor	5.3625	0	0	0	5.3625
18	OD144	Drift	5.5625	0.2	0	0	5.5625
19	IIBC3H04B	Monitor	5.5625	0	0	0	5.5625
20	OD145	Drift	5.7625	0.2	0	0	5.7625
21	IIBC3H04C	Monitor	5.7625	0	0	0	5.7625
22	OD146	Drift	6.35579	0.59329	0	0	6.35579
23	BDIP1	SBend	7.35579	1	0	-0.02523	7.35537
24	OD147	Drift	7.95816	0.60237	0	-0.05562	7.95697
25	IIBC3H05	Monitor	7.95816	0	0	-0.05562	7.95697
26	OD148	Drift	8.26816	0.31	0	-0.07126	8.26657
27	IUN3H05	Monitor	8.26816	0	0	-0.07126	8.26657
28	OD149	Drift	8.57816	0.31	0	-0.0869	8.57618
29	IIBC3H05A	Monitor	8.57816	0	0	-0.0869	8.57618
30	OD150	Drift	8.89756	0.3194	0	-0.10301	8.89517
31	KMBD3H05V	Kicker	8.89756	0	0	-0.10301	8.89517
32	OD151	Drift	9.72789	0.83033	0	-0.1449	9.72445
33	BDIP2	SBend	10.72789	1	0	-0.17139	10.724
34	IMIDPT	Monitor	10.72789	0	0	-0.17139	10.724
35	BDIP2	SBend	11.72789	1	0	-0.14993	11.72367
36	OD152	Drift	12.03358	0.30568	0	-0.13605	12.02904
37	KMAP3H07H	Kicker	12.03358	0	0	-0.13605	12.02904
38	OD153	Drift	12.32808	0.2945	0	-0.12267	12.32324
39	IIPM3H07A	Monitor	12.32808	0	0	-0.12267	12.32324
40	OD154	Drift	12.58106	0.25298	0	-0.11118	12.57596
41	IHA3H07A	Monitor	12.58106	0	0	-0.11118	12.57596
42	OD155	Drift	13.28166	0.7006	0	-0.07935	13.27583
43	IIPM3H07B	Monitor	13.28166	0	0	-0.07935	13.27583
44	OD156	Drift	13.54396	0.2623	0	-0.06744	13.53786
45	IIBC3H07	Monitor	13.54396	0	0	-0.06744	13.53786
46	OD157	Drift	13.77135	0.22739	0	-0.05711	13.76502
47	IYG3H07	Monitor	13.77135	0	0	-0.05711	13.76502
48	OD158	Drift	13.98522	0.21387	0	-0.04739	13.97867
49	IHA3H07B	Monitor	13.98522	0	0	-0.04739	13.97867
50	OD159	Drift	14.2442	0.25898	0	-0.03563	14.23738
51	IIPM3H07C	Monitor	14.2442	0	0	-0.03563	14.23738
52	OD160	Drift	14.4682	0.224	0	-0.02545	14.46115
53	IVBV3H07	Monitor	14.4682	0	0	-0.02545	14.46115
54	OD161	Drift	15.28134	0.81314	0	0.01148	15.27345
55	BSOL1	SBend	15.53134	0.25	0	0.02	15.5233
56	IPIVOTC	Monitor	15.53134	0	0	0.02	15.5233
57	BSOL1	SBend	15.78134	0.25	0	0.02283	15.77328
58	OD162	Drift	35.90434	20.123	0	0.02178	35.89628
59	IIPM3H08	Monitor	35.90434	0	0	0.02178	35.89628
60	OD163	Drift	41.40734	5.503	0	0.02149	41.39928
61	IIPM3H09	Monitor	41.40734	0	0	0.02149	41.39928
62	OD164	Drift	42.34564	0.9383	0	0.02144	42.33758
63	IITV3H10	Monitor	42.34564	0	0	0.02144	42.33758
64	OD165	Drift	48.35134	6.0057	0	0.02113	48.34328
65	IIDP3H10	Monitor	48.35134	0	0	0.02113	48.34328
66	OD166	Drift	53.05134	4.7	0	0.02088	53.04328
67	IITV3H10A	Monitor	53.05134	0	0	0.02088	53.04328
68	OD167	Drift	53.22134	0.17	0	0.02087	53.21328
69	IIDW3H10	Monitor	53.22134	0	0	0.02087	53.21328
70	OD168	Drift	66.91134	13.69	0	0.02016	66.90328
71	DIIBD3H10	Drift	69.91134	3	0	0.02	69.90328
72	IIBD3H10	Monitor	69.91134	0	0	0.02	69.90328
73	END	Marker	69.91134	0	0	0.02	69.90328

Table 3: Pass 5 Floor Coordinates (Universe 3)

Index Units	Name	Type	s m	l m	X m	Y m	Z m
0	BEGINNING	Beginning_Ele	0	—	0	0	0
1	IIPM3H02	Monitor	0	0	0	0	0
2	OD136	Drift	0.07214	0.07214	0	0	0.07214
3	KMBD3H02V	Kicker	0.22214	0.15	0	0	0.22214
4	OD137	Drift	0.26733	0.04519	0	0	0.26733
5	KMBD3H02H	Kicker	0.41733	0.15	0	0	0.41733
6	OD138	Drift	0.90622	0.48889	0	0	0.90622
7	KMFR3H03H	Kicker	0.90622	0	0	0	0.90622
8	OD139	Drift	1.31245	0.40623	0	0	1.31245
9	KMFR3H03V	Kicker	1.31245	0	0	0	1.31245
10	OD140	Drift	1.77586	0.46341	0	0	1.77586
11	KMFR3H04H	Kicker	1.77586	0	0	0	1.77586
12	OD141	Drift	2.18209	0.40623	0	0	2.18209
13	KMFR3H04V	Kicker	2.18209	0	0	0	2.18209
14	OD142	Drift	2.4805	0.29841	0	0	2.4805
15	IIPM3H04	Monitor	2.4805	0	0	0	2.4805
16	OD143	Drift	5.3625	2.882	0	0	5.3625
17	IIBC3H04A	Monitor	5.3625	0	0	0	5.3625
18	OD144	Drift	5.5625	0.2	0	0	5.5625
19	IIBC3H04B	Monitor	5.5625	0	0	0	5.5625
20	OD145	Drift	5.7625	0.2	0	0	5.7625
21	IIBC3H04C	Monitor	5.7625	0	0	0	5.7625
22	OD146	Drift	6.35579	0.59329	0	0	6.35579
23	BDIP1	SBend	7.35579	1	0	-0.01973	7.35553
24	OD147	Drift	7.95816	0.60237	0	-0.0435	7.95743
25	IIBC3H05	Monitor	7.95816	0	0	-0.0435	7.95743
26	OD148	Drift	8.26816	0.31	0	-0.05573	8.26719
27	IUN3H05	Monitor	8.26816	0	0	-0.05573	8.26719
28	OD149	Drift	8.57816	0.31	0	-0.06797	8.57695
29	IIBC3H05A	Monitor	8.57816	0	0	-0.06797	8.57695
30	OD150	Drift	8.89756	0.3194	0	-0.08057	8.8961
31	KMBD3H05V	Kicker	8.89756	0	0	-0.08057	8.8961
32	OD151	Drift	9.72638	0.82882	0	-0.11327	9.72427
33	BDIP2	SBend	10.72638	1	0	-0.13376	10.724
34	IMIDPT	Monitor	10.72638	0	0	-0.13376	10.724
35	BDIP2	SBend	11.72638	1	0	-0.11629	11.72379
36	OD152	Drift	12.03059	0.30421	0	-0.1052	12.02779
37	KMAP3H07H	Kicker	12.03059	0	0	-0.1052	12.02779
38	OD153	Drift	12.32509	0.2945	0	-0.09447	12.3221
39	IIPM3H07A	Monitor	12.32509	0	0	-0.09447	12.3221
40	OD154	Drift	12.57807	0.25298	0	-0.08525	12.57491
41	IHA3H07A	Monitor	12.57807	0	0	-0.08525	12.57491
42	OD155	Drift	13.27867	0.7006	0	-0.05971	13.27505
43	IIPM3H07B	Monitor	13.27867	0	0	-0.05971	13.27505
44	OD156	Drift	13.54097	0.2623	0	-0.05015	13.53717
45	IIBC3H07	Monitor	13.54097	0	0	-0.05015	13.53717
46	OD157	Drift	13.76836	0.22739	0	-0.04187	13.76441
47	IYG3H07	Monitor	13.76836	0	0	-0.04187	13.76441
48	OD158	Drift	13.98223	0.21387	0	-0.03407	13.97814
49	IHA3H07B	Monitor	13.98223	0	0	-0.03407	13.97814
50	OD159	Drift	14.24121	0.25898	0	-0.02463	14.23695
51	IIPM3H07C	Monitor	14.24121	0	0	-0.02463	14.23695
52	OD160	Drift	14.46521	0.224	0	-0.01647	14.4608
53	IVBV3H07	Monitor	14.46521	0	0	-0.01647	14.4608
54	OD161	Drift	15.27835	0.81314	0	0.01317	15.2734
55	BSOL1	SBend	15.52835	0.25	0	0.02	15.5233
56	IPIVOTC	Monitor	15.52835	0	0	0.02	15.5233
57	BSOL1	SBend	15.77835	0.25	0	0.02227	15.77329
58	OD162	Drift	35.90135	20.123	0	0.02143	35.89629
59	IIPM3H08	Monitor	35.90135	0	0	0.02143	35.89629
60	OD163	Drift	41.40435	5.503	0	0.0212	41.39929
61	IIPM3H09	Monitor	41.40435	0	0	0.0212	41.39929
62	OD164	Drift	42.34265	0.9383	0	0.02116	42.33759
63	IITV3H10	Monitor	42.34265	0	0	0.02116	42.33759
64	OD165	Drift	48.34835	6.0057	0	0.0209	48.34329
65	IIDP3H10	Monitor	48.34835	0	0	0.0209	48.34329
66	OD166	Drift	53.04835	4.7	0	0.02071	53.04329
67	IITV3H10A	Monitor	53.04835	0	0	0.02071	53.04329
68	OD167	Drift	53.21835	0.17	0	0.0207	53.21329
69	IIDW3H10	Monitor	53.21835	0	0	0.0207	53.21329
70	OD168	Drift	66.90835	13.69	0	0.02013	66.90329
71	DIIBD3H10	Drift	69.90835	3	0	0.02	69.90329
72	IIBD3H10	Monitor	69.90835	0	0	0.02	69.90329
73	END	Marker	69.90835	0	0	0.02	69.90329

Proof of principle design for pre-chicane for use with 5T transverse solenoid for high current in Hall C, small SHMS angles in Hall C, or SoLID

Jay Benesch
23 February 2024

Discussion

Two proposals planned for PAC52 require the use of the new 5T polarized target solenoid. One uses it with full transverse field. The other uses it twisted 21° from longitudinal so Bx component is 38.4% of nominal. $\int B dL = 1.3415E6$ G-cm over $[-100,100]$ cm with most of the field within $[-25,25]$ cm. These two proposals require current under 100 nA. Total power is less than 1100 W at 11 GeV. It follows that the discussion in <https://jlabdoc.jlab.org/docushare/dsweb/View/Collection-56294> Examination of the need for an upstream chicane for proposal "A Measurement of the Proton g_2 Structure Function at Intermediate Q²" still obtains for these *as long as SHMS need not attain small angles*. A local beam dump mounted from the floor of the hall suffices given the existence of the 2 cm vertical chicane in Hall C beam line for height fine tuning.

For SoLID or experiments in Hall C which require the use of SHMS at small angle one will need a pre-chicane. SoLID extends over 10 m beyond the target so even with low current the beam will intersect things it shouldn't within the system if the bending from a transverse field, be it from a polarized target or another system, is not compensated. High current beams have to make it to the beam dump in the dump tunnel in both halls. Small angle use of SHMS requires a beam pipe which fits in notches in the magnets, not one pointing towards a beam dump on the floor.

I approximate the transverse solenoid as two horizontal dipoles of 25 cm length with the pivot located between them; no gap between the dipoles. Field of each dipole is then 26.84 kG for BdL given above. Figure 2 has the actual field.

A 5T transverse target has not been used in Hall C since the Compton polarimeter was installed for Qweak. I found an Optim file from 2000 written by either Alex Bogacz or Valeri Lebedev which used built-in header functionality I never touch to compute the chicane. The chicane was 19 m long and there is only about 9 meters available given Compton polarimeter so I did not attempt to decipher the old file. I simply adapted my existing Hall C Optim files and used dead reckoning to arrive at rough solutions for second, fourth and fifth pass, described below. The fields for the chicane dipoles remain roughly constant because the 5T solenoid is fixed. For the case with 21° rotation, the chicane dipole fields will be about 38% of those shown below.

There are four constraints and four variables, two fields and two drifts. The constraints are the linked (x,z) position at the pivot, the height at the pivot, and the vertical angle of the beam after it leaves the far field of the target magnet. The target has vertical motion so getting within a cm there suffices and proved possible. The thinned region of the dump face is a few cm in diameter so getting that Y value dead on isn't necessary either, aka exit angle can vary slightly. (x,z) constraints are most important and are linked because there are no horizontal dipoles after the alcove. There are two drifts available as variables, the one between the two dipoles and the one between the second dipole and the 5T solenoid. I tried both. Using the first keeps the center of the center dipole closer to stationary in (x,z) but not perfectly. I ended up using just the two fields and the drift between the dipoles.

The existing 1 m vertical dipole MBE3H05 must be replaced with one capable of 15.5 T. The existing 1 meter dipoles MBE3H06 and MBE3H07 are to be replaced with a 2 m dipole capable of 14.5 T.

While the FZ magnet used for the 2000 chicane has enough steel to reach the necessary BdL, the coils may melt. The 1 meter MBE cannot be pushed that hard. I suggest new magnets be fabricated with the cross-section defined for the FFA 20+ GeV hall lines which evolved in TNs 21-051 (380 cm), 22-022 (200 cm) and 23-008 (180 cm). It is likely that a new coil can be designed for the FZ steel but I have chosen not to attempt this. It seems to me better to prototype the new design and measure it as part of preparation for the energy upgrade.

Five files are attached: a spreadsheet with the orbits for three passes in which I prepared the plot and tables below, three Optim files and a spreadsheet with 2010 modeling results for the FZ. Yves Roblin of CASA has scripts to turn Optim into elegant files in which they or others competent in accelerator physics (as I am not) can refine the design. Among the choices I made which will have to be revisited are removing the entrance and exit focusing terms from the chicane dipoles. An attempt to keep the second (2m) dipole better centered in (x,z) than the cm span shown below should also be made to ease mechanical engineering requirements. If one wants to get fancy one should use the actual solenoid field instead of the dipole approximation in refining the model but that wasn't necessary in 4/6 GeV days. Again, this is a proof of principle exercise.

Table 1: positions in accelerator coordinates

	name	S[cm]	X[cm]	Y[cm]	Z[cm]	TetaY[deg]	Energy[Mev]
Pass 2	2m_midpt	13981.977	-12170.965	9962.490	-38450.090	-0.383	4483
Pass 4	2m_midpt	13979.567	-12170.247	9980.257	-38449.155	-0.167	8843
Pass 5	2m_midpt	13979.267	-12170.155	9983.809	-38449.035	-0.125	11023
nominal	iPIVOTC	14458.568	-12462.200	9999.800	-38829.405	0	11023
Pass 2	iPIVOTC	14461.803	-12462.198	10000.060	-38829.402	2.563	4483
Pass 4	iPIVOTC	14459.393	-12462.204	9999.462	-38829.409	1.315	8843
Pass 5	iPIVOTC	14459.093	-12462.200	9999.285	-38829.405	1.063	11023
nominal	END	19896.568	-15773.908	9999.800	-43142.691	0	11023
Pass 2	END	19899.803	-15773.901	9999.894	-43142.682	-0.008	4483
Pass 4	END	19897.393	-15773.910	10000.852	-43142.694	0.012	8843
Pass 5	END	19897.093	-15773.907	10001.139	-43142.690	0.017	11023

Table 1 shows that I got close to nominal values with dead reckoning both at the pivot and at the end of the dump tunnel. Beam height variation at the pivot will be taken into account with vertical target motion over an 8 mm range or improved by further work by others. Small angles remain so the beam is not perfectly centered on the dump face but it's close enough given the diameter of the thin region of the dished head. Fields in the chicane dipoles vary slightly for the three designs, within a 2% span, for full transverse field. For the 21° case, all scale.

Table 2: ∫BdL for chicane dipoles

	1 m G-cm	2 m G-cm	solenoid
Pass 2	-1540000	2880000	-1342000
Pass 4	-1520000	2868000	-1342000
Pass 5	-1513000	2866000	-1342000

Note that there is 54 m from pivot to end of dump tunnel. My magnet model ends ~18 m.

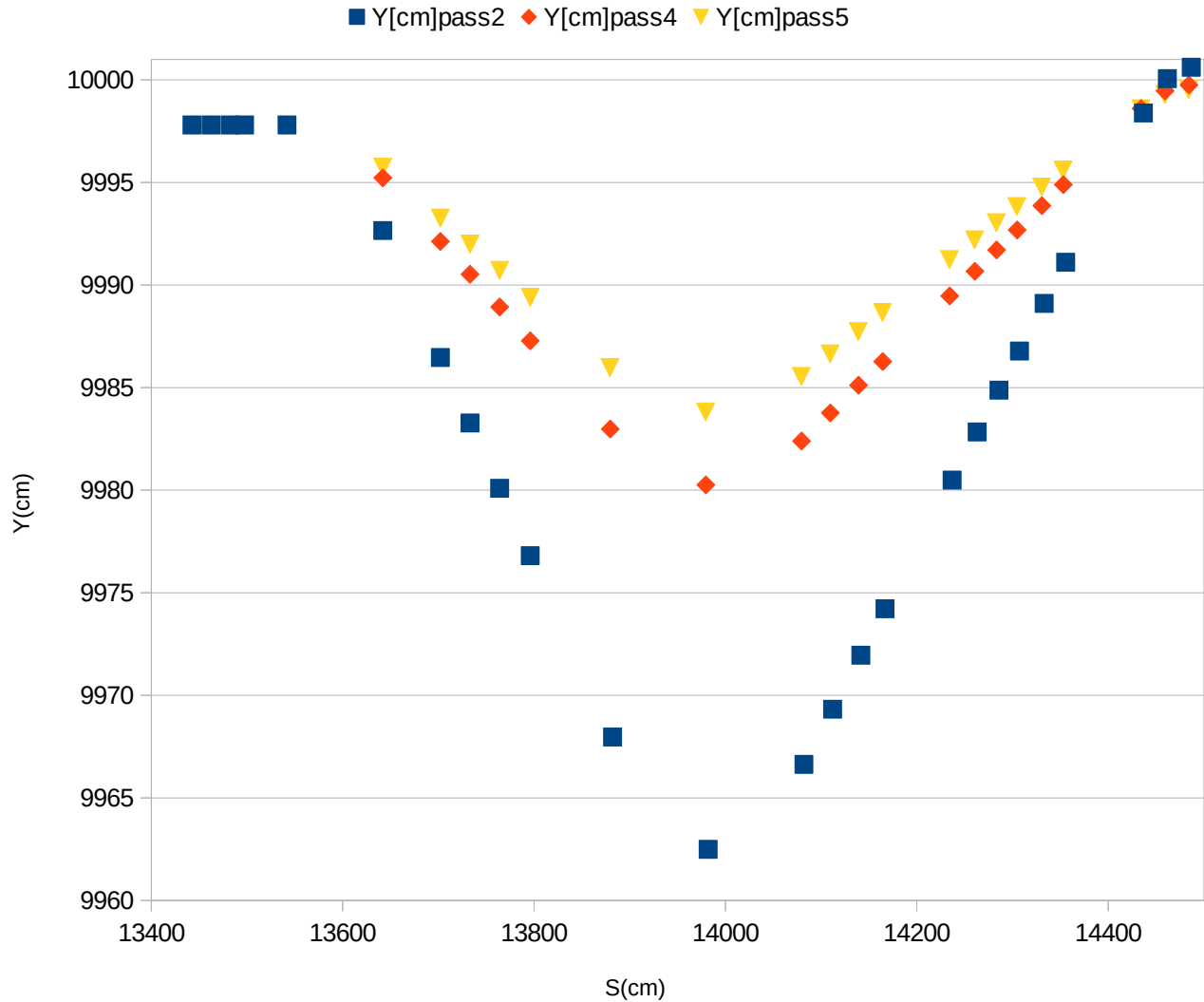


Figure 1 Vertical excursions in the chicane as a function of pass (beam energy). Pivot is at S~14460 as seen in Table 1.

Conclusion

It is possible to create an upstream chicane which will locate the beam at the pivot and at the beam dump. At least one new magnet and preferably two are required. Responsibility for the mechanical design to allow the vertical motion shown in Figure 1, the detailed magnet design and the detailed optics design rests elsewhere. This is just a proof of principle.

More Discussion

The Hall C beam leaves the Lambertson at $y=9997.8$ cm in accelerator coordinates. The pivot was built at 10000 cm in accelerator coordinates; it has settled to 9999.8 cm for experiments with the standard spectrometers. There is a 2 cm vertical chicane using two one-meter dipoles in the hall, followed by an unpowered one meter horizontal dipole. The space these occupy was used in this design. All diagnostics were left in existing positions. The diagnostic girders will have to be tilted to match beam path through the chicane.

In Hall A the MOLLER target is centered 5 m upstream of the pivot and is almost 2 m in diameter. SoLID will be placed about 5 m after the pivot. Since the chicane herein is less than 7 meters long there is sufficient room for it in Hall A for use with SoLID. Mechanical design is another question, as is the placement of diagnostics.

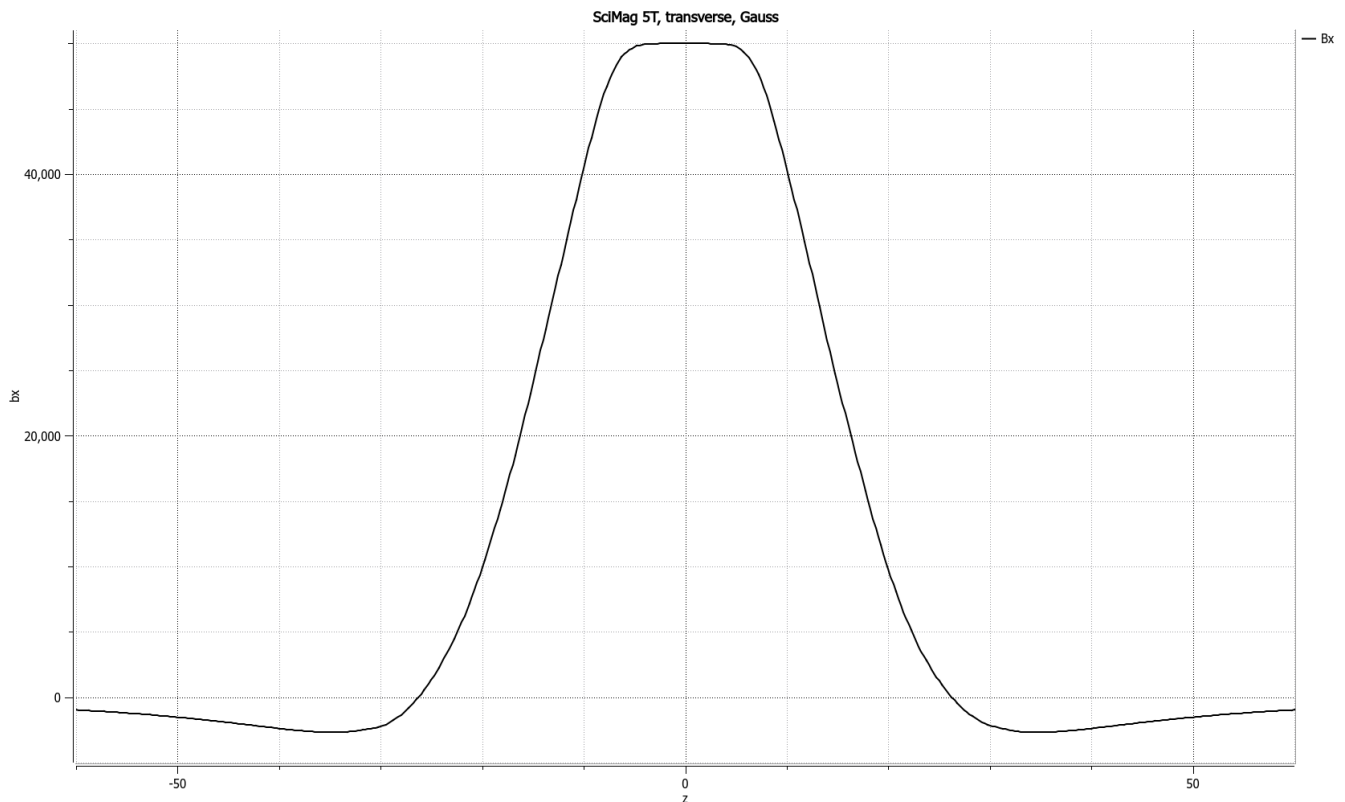


Figure 2. Field of solenoid in transverse mount, B_x (Gauss). As mentioned in the third paragraph of page 1, I approximated this as two dipoles 25 cm long with the zero-length pivot between them.

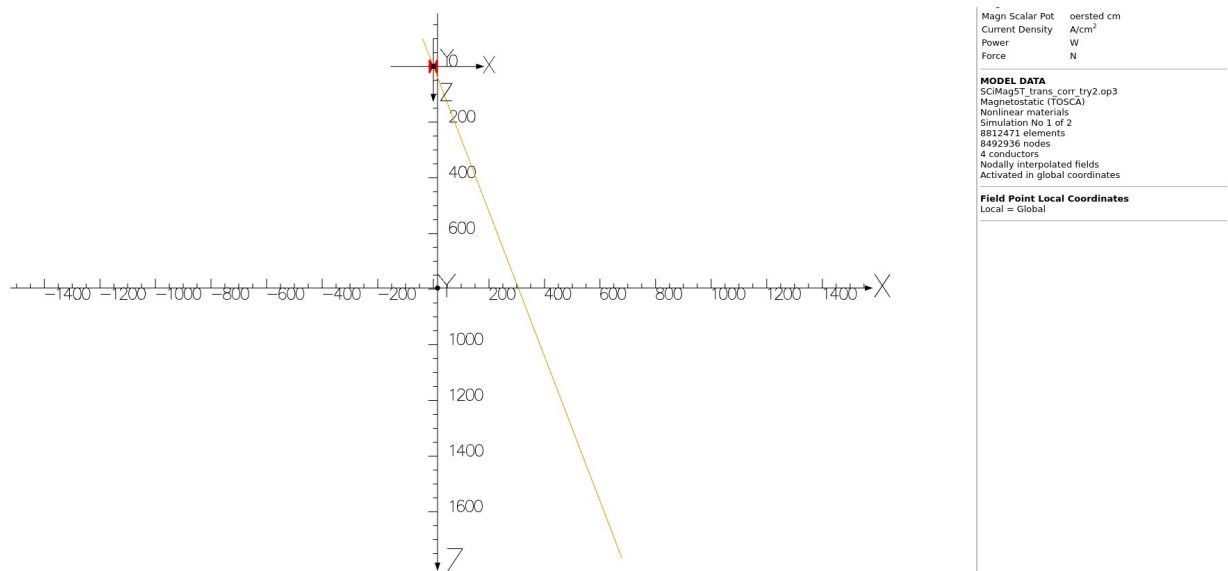


Figure 3. Top view of beam entering **transverse** solenoid at 21° angle as that's easier than making a new model. **This figure and the next four were created in error and are included because they exist. Rotated longitudinal solenoid figures 8-12. Full transverse figures 13 and 14.**

19/Feb/2024 15:46:18

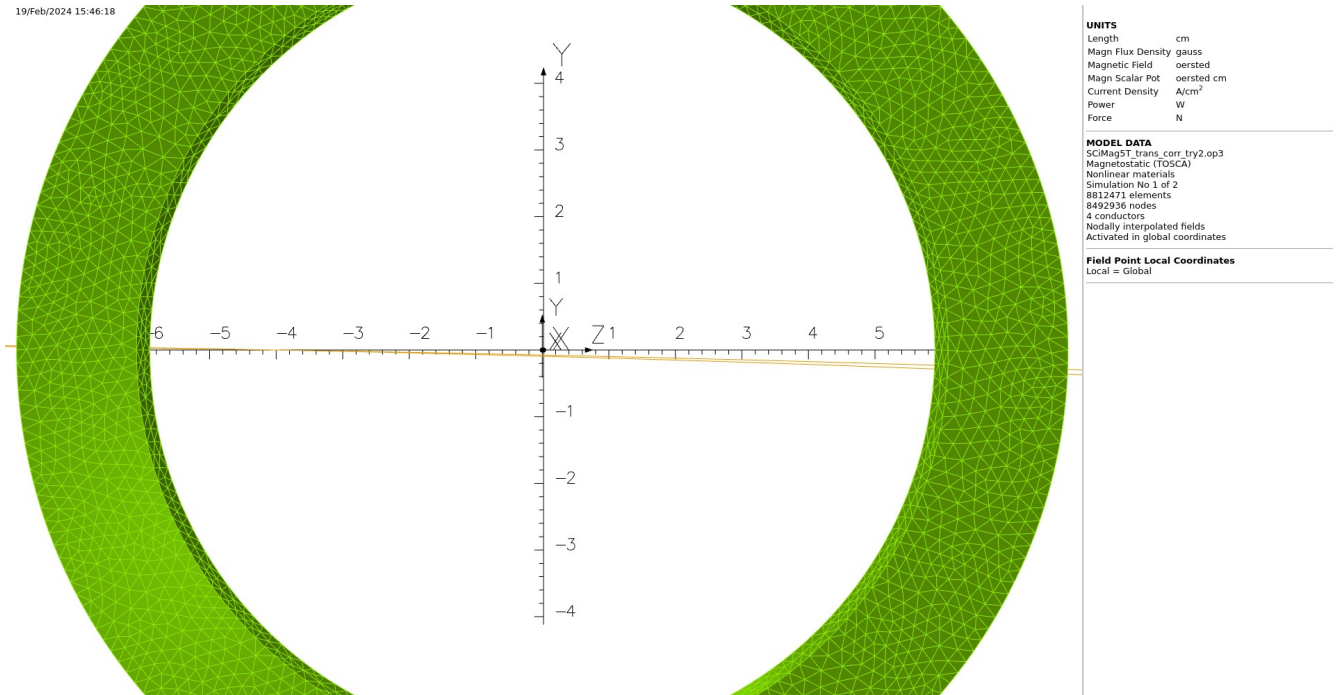


Figure 4. Side view of Figure 3 showing slight vertical deflection at center. 8.84 and 11 GeV beams.

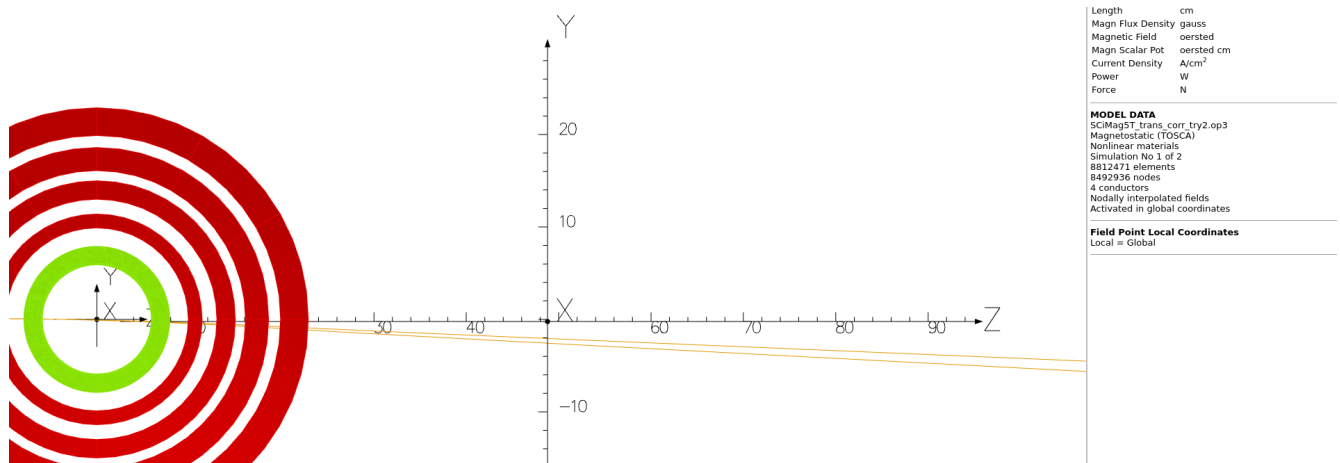


Figure 5. Side view of Figure 3 past end of target chamber. 7.5 cm diameter exit beam pipe desirable given scattered beam if no chicane is to be used. 5 cm possible given low current.

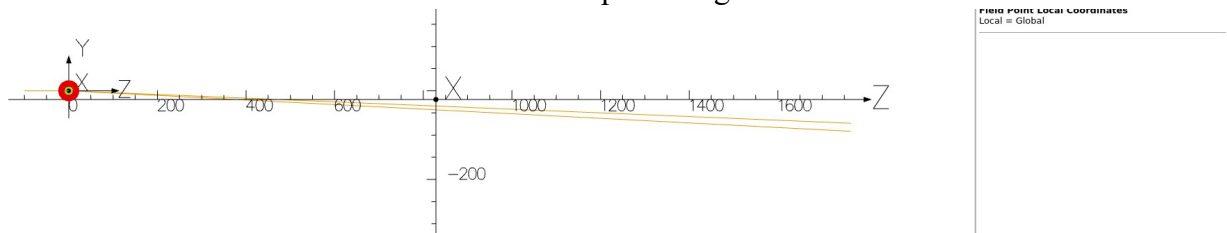


Figure 6. Side view of Figure 3 through the end of the model. 8.84 and 11 GeV beams

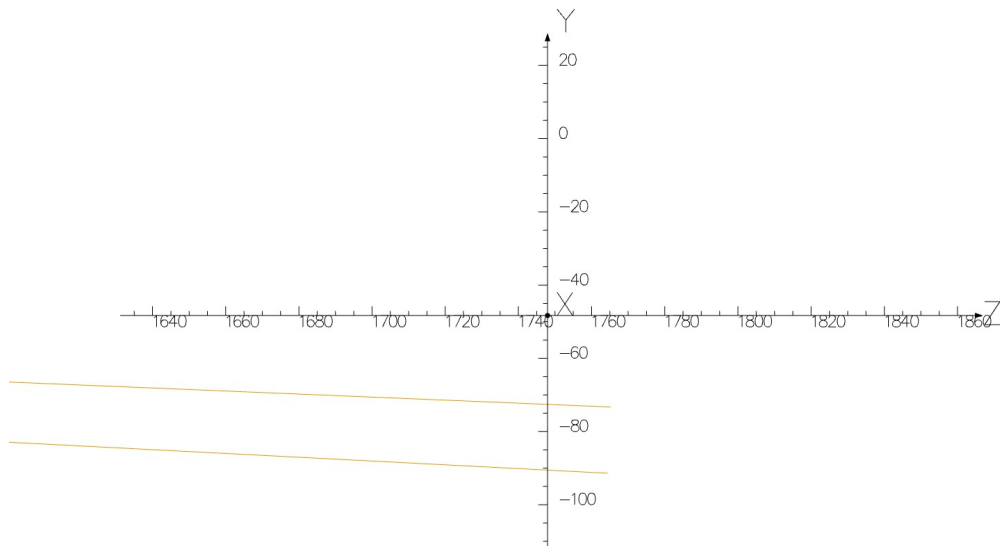


Figure 7. Side view of Figure 3, end of Fig. 6. 8.84 and 11 GeV beams.

Length	cm
Magn Flux Density	gauss
Magnetic Field	oersted
Magn Scalar Pot	oersted cm
Current Density	A/cm ²
Power	W
Force	N

MODEL DATA
 SCIMag5T_trans_corr_try2.op3
 Magnetostatic (TOSCA)
 Nonlinear materials
 Simulation No 1 of 2
 8812471 elements
 8492936 nodes
 4 conductors
 Nodally interpolated fields
 Activated in global coordinates

Field Point Local Coordinates
 Local = Global

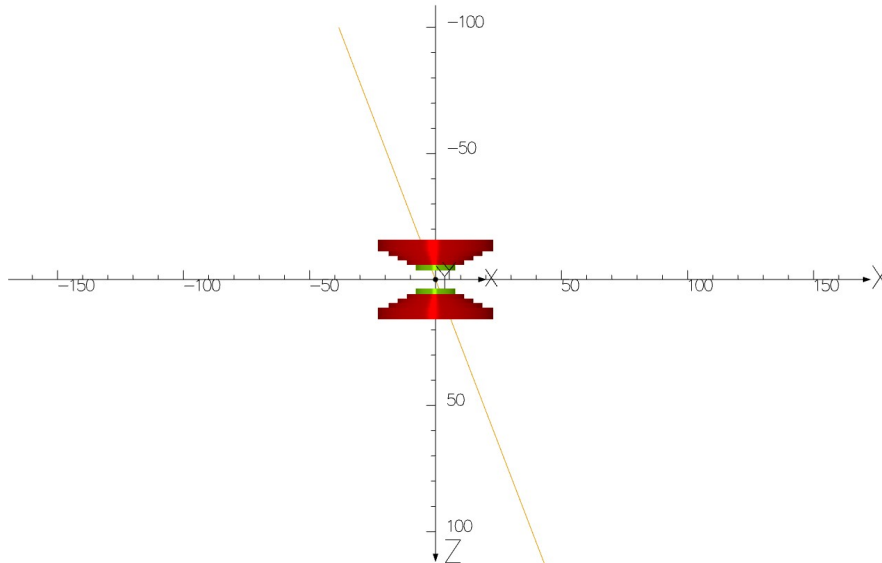


Figure 8 Top view of beam entering **longitudinal** solenoid at 21° angle

Length	cm
Magn Flux Density	gauss
Magnetic Field	oersted
Magn Scalar Pot	oersted cm
Current Density	A/cm ²
Power	W
Force	N

MODEL DATA
 SCIMag5T_long_corr_try2.op3
 Magnetostatic (TOSCA)
 Nonlinear materials
 Simulation No 1 of 2
 9602030 elements
 12446316 nodes
 4 conductors
 Nodally interpolated fields
 Activated in global coordinates
 8-fold rotational symmetry

Field Point Local Coordinates
 Local = Global

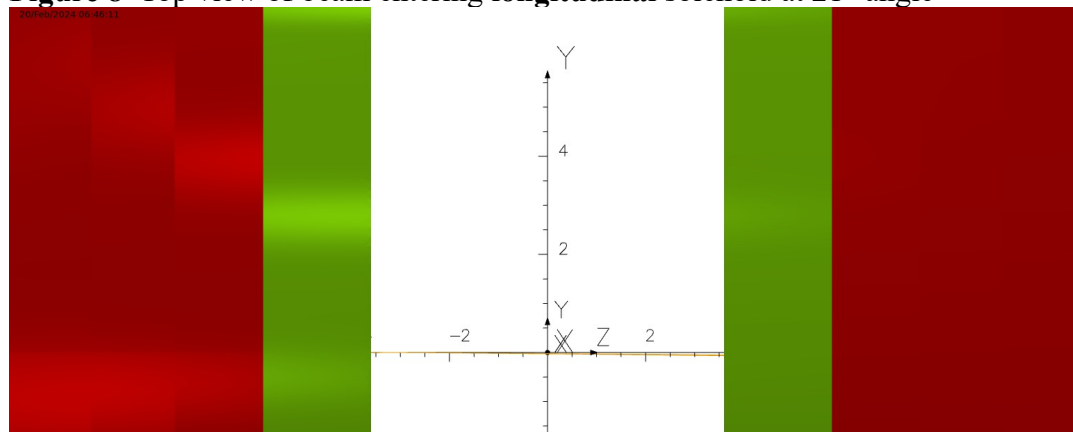


Figure 9. Side view of Fig. 8 with 8.84 and 11 GeV beams

Length	cm
Magn Flux Density	gauss
Magnetic Field	oersted
Magn Scalar Pot	oersted cm
Current Density	A/cm ²
Power	W
Force	N

MODEL DATA
 SCIMag5T_long_corr_try2.op3
 Magnetostatic (TOSCA)
 Nonlinear materials
 Simulation No 1 of 2
 9602030 elements
 12446316 nodes
 4 conductors
 Nodally interpolated fields
 Activated in global coordinates
 8-fold rotational symmetry

Field Point Local Coordinates
 Local = Global

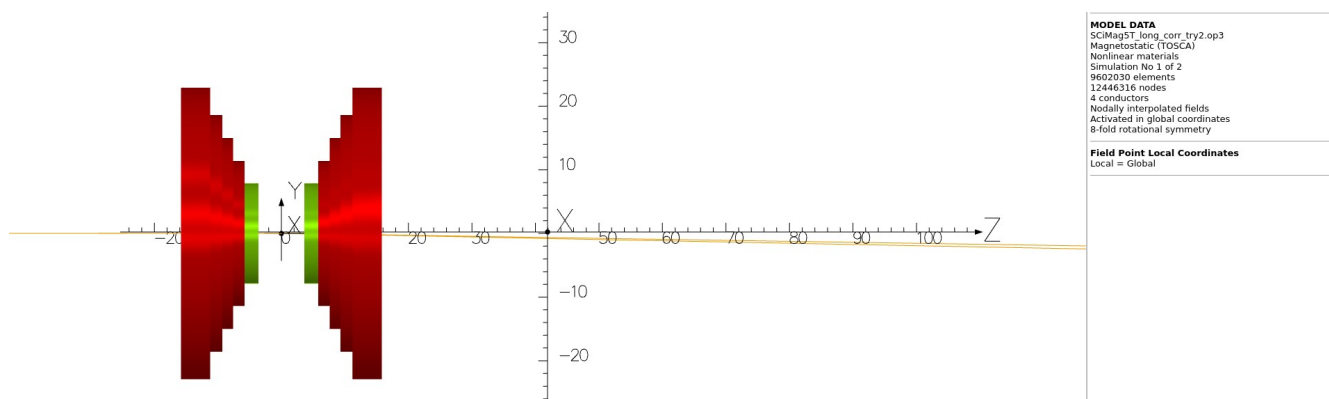


Figure 10. Side view of Fig. 8 with 8.84 and 11 GeV beams. About 1 cm deflection at exit of target chamber for unscattered beam so small beam pipe should suffice if the collaboration doesn't need SHMS to be too close to the beam line. Notches in SHMS magnets may be an issue.

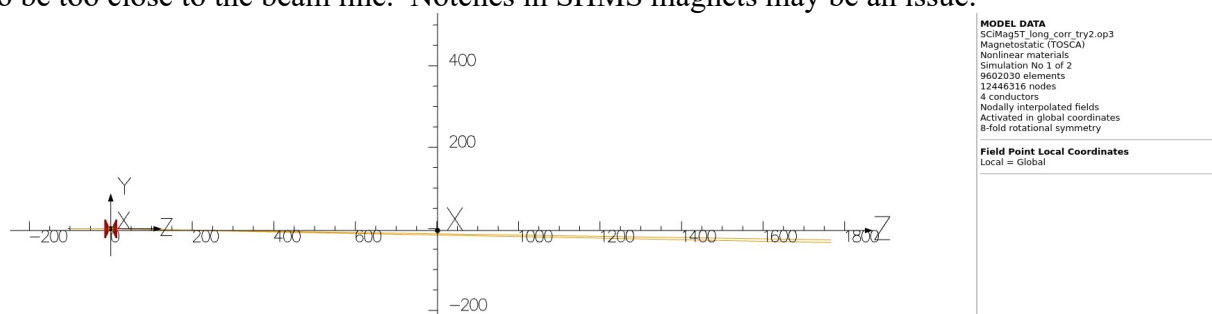


Figure 11. Side view of Fig. 8 with 8.84 and 11 GeV beams to end of model.

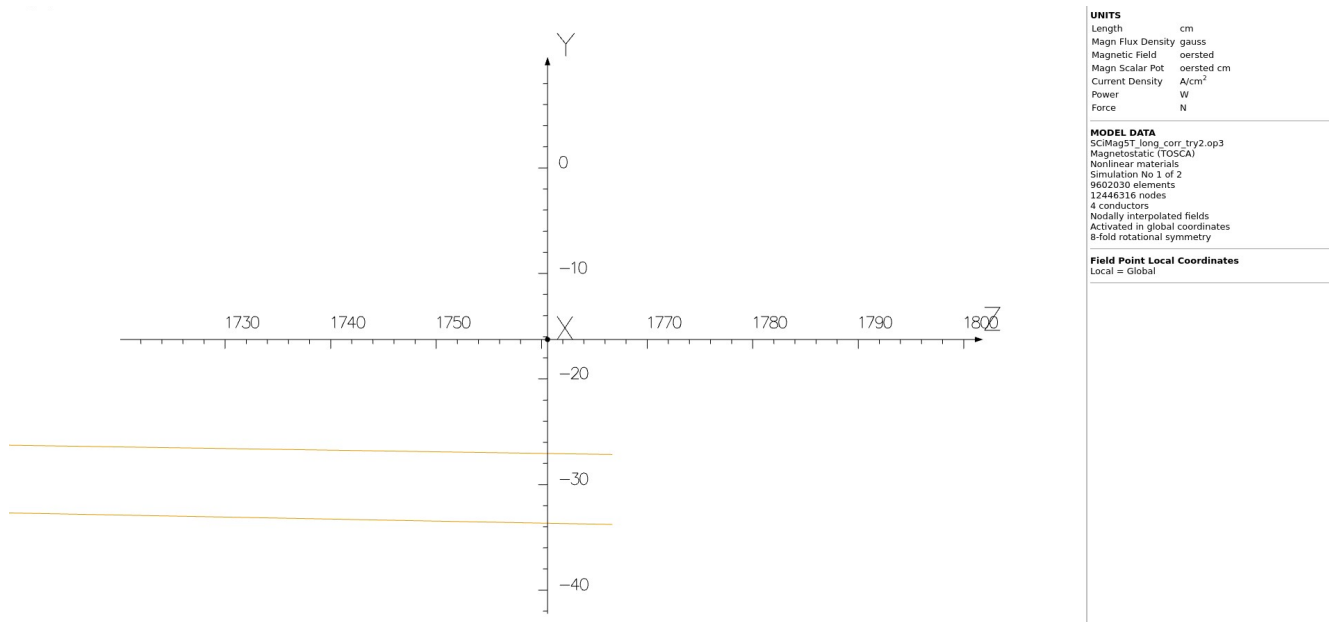


Figure 12. Side view of Fig. 8 with 8.84 and 11 GeV beams at end of model so one sees the difference in deflection.

The proposal cited in the first paragraph wants to use SHMS at small angles. It may be that the chicane will be necessary to allow this given the small exit beam pipe which fits in the notches in the SHMS magnets. The figures below shows 4.44 and 8.84 GeV beam going through the 5 T transverse magnet normal to the field.

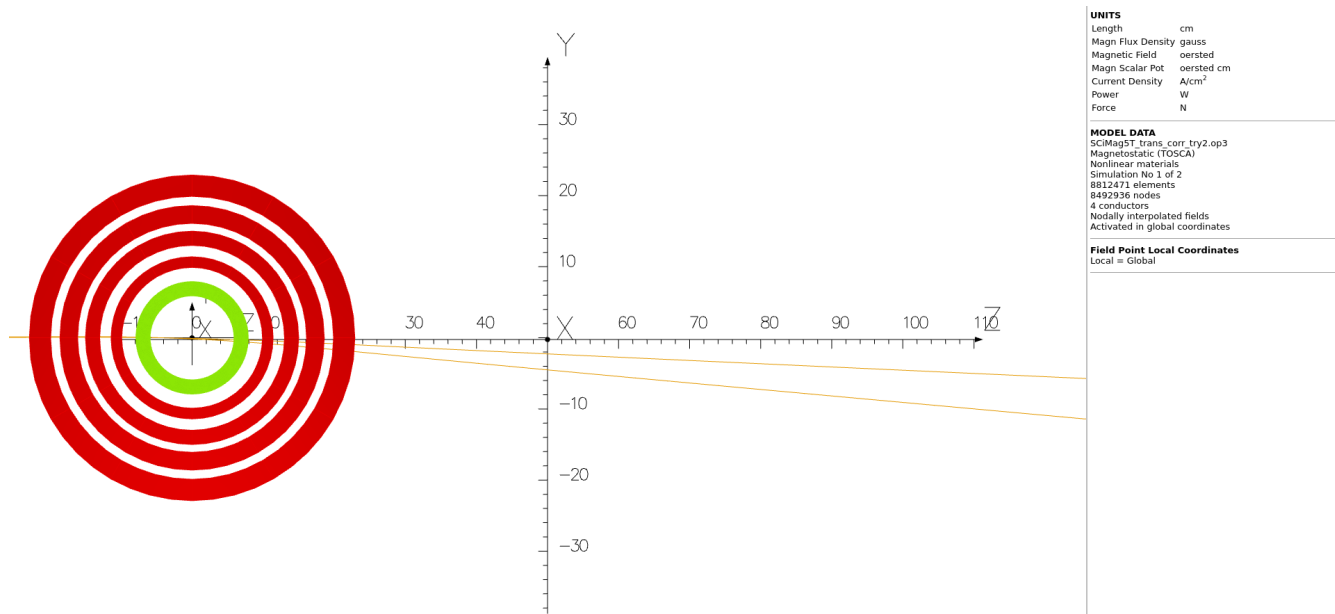


Figure 13. Side view of transverse magnet with 4.44 and 8.84 GeV beams. Axes cross at Z=50 cm because the target chamber is roughly 100 cm in diameter. The 4.44 GeV unscattered beam is a bit more than 4 cm below the axis. If memory serves this doesn't fit in the small beam pipe needed for SHMS at minimum angle.

20/Feb/2024 15:37:58

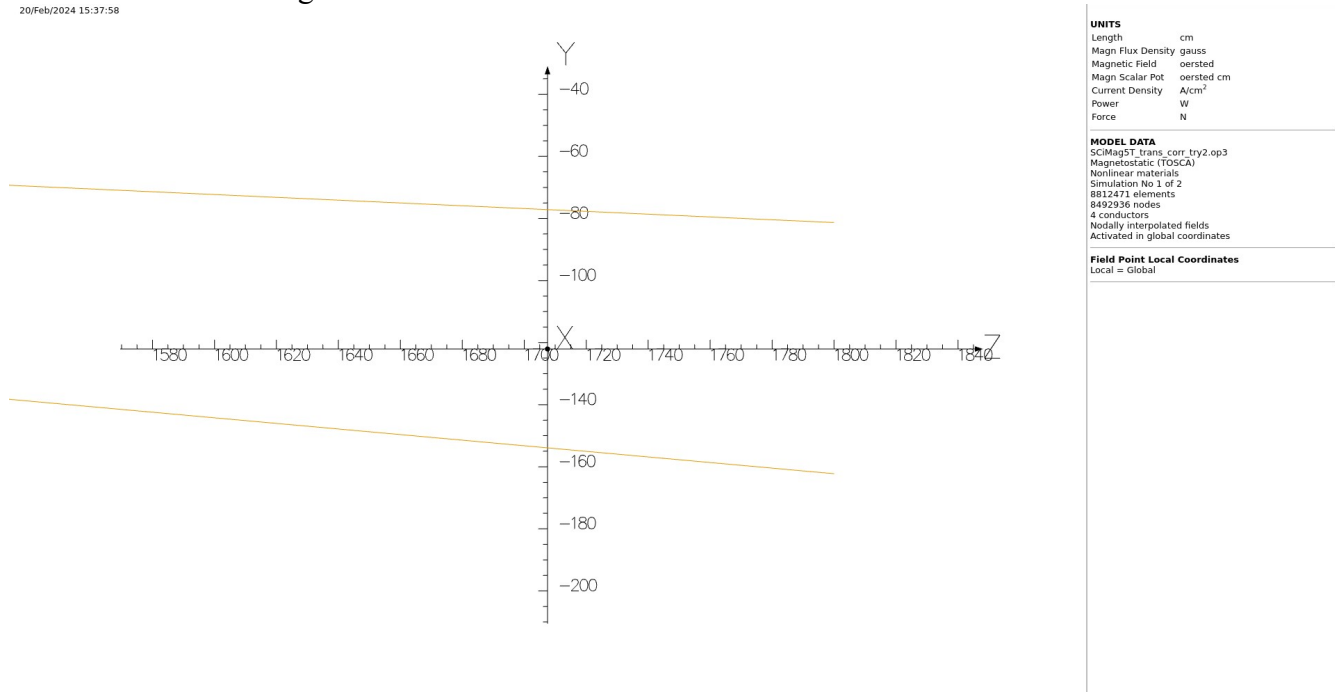


Figure 14. As Figure 13, 4.44 and 8.84 GeV beams at end of the magnet model. End wall of the hall is well beyond this but beam will not reach the floor starting 10' above it.

Conclusion Two

If low current experiments need to use the SHMS at small angle the chicane will be required.

Support column used ~2000 for 2m dipole is in Physics storage building

